N84-25203

NASA

Technical Memorandum 86101

Auroral Kilometric Radiation: Wave Modes, Harmonics and Source Region Electron Density Structures

Robert F. Benson

MAY 1984

National Aeronautics and
Space Administration

Goddard Space Flight Center
Greenbelt, Maryland 20771

Auroral Kilometric Radiation: Wave Modes, Harmonics and Source Region Electron Density Structures

Robert F. Benson

Laboratory for Planetary Atmospheres

NASA/Goddard Space Flight Center

Greenbelt, MD 20771

May 1984

Abstract

A number of dramatic changes are observed in the characteristics of auroral kilometric radiation (AKR) as the source region plasma to gyrofrequency ratio f_N/f_H varies from 0.1 to 1.3. Most notable of these is a change from right hand polarized extraordinary (X) mode AKR dominance to left hand ordinary mode (O) AKR dominance as f_N/f_H varies from smaller to larger values. In addition to the X and O mode AKR, Z (the slow branch of the X mode) and whistler (W) mode are also observed. The Z mode is observed over all f_N/f_H values, is often confined to the frequency region between f_N and f_H and is typically slightly less intense than the O mode. The W mode is confined to frequencies less than $f_H/2$, suggesting that it is the result of field-aligned ducted signals reaching the satellite from a source at lower altitudes. Harmonic AKR bands, which appear to be of natural rather than instrumental origin and appear to be associated with the O as well as the X mode, are commonly observed. The 2nd harmonic X mode appears to be due to propagating signals, whereas the higher harmonics appear to be confined to low density source regions. The 2nd harmonic associated with the O mode is observed mainly at frequencies above the ambient $2f_H$ value when f_N/f_H is large and below $2f_H$ when f_N/f_H is small. The observations were obtained from some 200 ionograms from 12 passes of the ISIS 1 satellite through AKR source regions. Electron density contours from the satellite altitude down to the altitude of the F layer ionization peak were obtained from the sounder data on each pass. Source encounters were made on nearly all of these passes and both the minimum AKR source altitudes and the corresponding f_N/f_H values (which correspond to maximum values) were determined. The deduced $(f_N/f_H)_{max}$ is always less than 0.4 and is typically less than 0.2 during the generation of X-mode AKR. For O-mode AKR, on the other hand, $(f_N/f_H)_{max}$ approaches 0.9.

The corresponding AKR source region minimum altitudes extend down to 2400 km. The $(f_N/f_H)_{max}$ values are in excellent agreement with previously published results of the maximum instability temporal growth rates, obtained from the AKR Doppler shifted cyclotron mechanism, as a function of f_N/f_H. The latitudinal extent of the low density, i.e., $N_e < 100$ cm^{-3}, AKR source regions ranged from a few degrees to more than 20^o along the satellite orbit (88^o inclination). Within the wide density depletions, i.e., those that extended over many degrees, there were no large enhancements of the ambient f_N/f_H value. These results, which were limited by the ~100 km spatial resolution corresponding to the spacing between topside sounder ionograms, were substantiated on a much finer spatial scale (~10 km for N_e or 1/10 km for ΔN_e) using in situ data from the on-board Langmuir probe which were available for 10 of the 12 passes. The observed lack of large density enhancements within AKR source region density cavities provides additional confidence that the observed intense AKR is cyclotron X-mode radiation rather than plasma frequency O-mode radiation. The observed N_e enhancements, however, were larger than those required to support a feedback mechanism in the source region.

CONTENTS

1. Introduction

Auroral kilometric radiation (AKR) is an intense electromagnetic emission originating high above the auroral regions which is associated with discrete auroral arcs. This association was convincingly demonstrated in the classic work of Gurnett [1974] based on the plasma wave data from the Imp 6 and 8 spacecraft and auroral photographs from the U.S. Air Force Dapp satellite. The intensity of the emission (up to 10^9 W), and the likely relevance of the generation mechanism to other astrophysical radio sources, has motivated a high level of observational and theoretical interest over the last decade - as revealed in the recent review by Gurnett [1983].

Of particular importance to the present work is the data from the ionospheric sounder on the ISIS 1 satellite. High latitude nighttime data collected near apogee (3500 km) from this satellite have provided a wealth of AKR source region information based on the high frequency-resolution available from the swept-frequency sounder receiver between 100 kHz and 2MHz, which records naturally occurring AKR, and the sounder-derived electron density N_e profiles extending from the satellite altitude to the height of the ionization peak of the F layer. The first paper on AKR using ISIS 1 data [Benson and Calvert, 1979] presented evidence on the following aspects of the radiation: (1) it is generated in the extraordinary mode just above the local cut-off frequency, (2) it emanates nearly perpendicular to the magnetic field $\vec{B}$ and is refracted in the upward direction, (3) it originates within local N_e depletions which can extend down to the vicinity of about 2000 km, (4) it is observed above the nighttime auroral zone over a wider extent in longitude than in latitude with an intense source region observed most often near 2200 magnetic local time and 70^o invariant latitude, and (5) it is directly related to inverted V electron precipitation events with an electron-to-wave energy

conversion efficiency of the order of 0.1 to 1%. James [1980] used the spin-modulated noise as received by the ISIS 1 dipole, combined with ray tracing calculations, to deduce that the AKR was generated nearly perpendicular to $\vec{B}$, but downward, and then refracted upward. It is this upward refraction from an altitude distributed AKR source (with frequency increasing with decreasing altitude) that gives rise to the characteristic AKR signature on a series of ISIS 1 ionograms, i.e., the variable gap between the AKR minimum frequency and the ambient electron cyclotron frequency as the satellite penetrates the AKR source region [Benson and Calvert, 1979; Calvert, 1981a]. Simultaneous observations from the topside sounder and the soft particle spectrometer onboard ISIS 1 indicated that in order to generate AKR it is necessary to have N_e depletions together with inverted V electron precipitation with energy distribution functions near the inverted V center containing positive slopes in the keV energy range [Benson et al., 1980]. The latitudinal widths of the N_e cavities, as determined from in situ measurements along the satellite tracks, for the AKR events investigated in the above papers have been presented in the review paper by Benson [Figure 12, 1981]. Evidence supporting a natural origin for the harmonic AKR bands first reported by Benson and Calvert [1979] was presented by Benson [1982a]. An ISIS 1/Alaskan all-sky camera station correlative study of AKR, topside N_e structures and the visual aurora indicated that intense AKR is highly correlated with bright aurora and that the N_e cavities above about 2000 km altitude, which are required for the generation of intense AKR, can have a far greater latitudinal extent than either the region containing auroral-arc field-lines or the AKR source region [Benson and Akasofu, 1984]. Benson [1984] presented examples of ordinary mode AKR (with harmonics) as observed in regions of relatively high N_e, i.e., high relative to the N_e cavities associated with the source regions of the more intense extraordinary mode AKR.

The above ISIS 1 observations have been of major significance to a number of theoretical studies starting with the pivotal paper of Wu and Lee [1979]. An essential ingredient in their electron cyclotron maser mechanism for the generation of AKR was the locally depleted N_e cavity observed by ISIS 1 [Benson and Calvert, 1979]. These observations also supported the Wu and Lee prediction that AKR would be generated in the extraordinary mode just above the local cutoff frequency. This dominance of the extraordinary (X) mode over the ordinary (O) mode in AKR has also been inferred from (1) ray tracing calculations of AKR detected by more distant satellites (Hawkeye, IMP6 and IMP8) by Green et al. [1977], (2) the AKR low frequency cutoff at the ambient electron gyrofrequency detected during AKR source region encounters by Hawkeye [Gurnett and Green, 1978], direct polarization measurements made from the two Voyager spacecraft on their way to the outer planets [Kaiser et al., 1978] and (4) direct polarization measurements made from the high altitude polar orbiting DE-1 satellite [Shawhan and Gurnett, 1982]. These observational results pertaining to wave polarization have been challenged by Oya and Morioka [1983] based on observations from the Jikiken satellite (EXOS-B) and their mode-conversion theory. Their observations indicate that AKR is in the Z mode (ionospheric notation for the low frequency slow branch of the X mode) and the O mode, and they present arguments that all other AKR observations previously interpreted as X mode could consistently be explained in terms of O mode signals. Their mode-conversion theory assumes that AKR originates as electrostatic waves which are converted first to the Z mode and then to the O mode. This theory required the presence of specific N_e gradients as do the similar mode-conversion mechanisms proposed by Jones [1977] and Jones et al. [1984]. The required density enhancements in these mode-conversion mechanisms to produce O mode AKR are much greater than those called for in the recent

feedback model proposed by Calvert [1982]. This model generates X mode signals in a form that can explain the fine-structure first revealed in the AKR frequency spectrum by Gurnett et al. [1979] using ISEE 1 data.

There is no question concerning the identification of the Jikiken-observed emissions as O and Z mode AKR, but there is a major question concerning the relative importance of the X, O and Z modes in the AKR process. High latitude O and Z mode emissions have been observed from a number of satellites. The AKR observed by Voyagers 1 and 2 was predominately (80%) in the X mode but on a few occasions the O mode signals were clearly stronger than the X mode signals [Kaiser et al., 1978]. The DE 1 observations are consistent with the presence of an O mode component with a power level 17 dB below the X mode component [Shawhan and Gurnett, 1982]. The ISIS 1 observations indicate that the intensity of O mode AKR can exceed the X mode intensity when the spacecraft is out of the low density cavities associated with intense X mode AKR. A comparison of the maximum power levels of the two modes, however, indicates that the most intense O mode is typically 30 dB less than the most intense X mode AKR [Benson, 1984]. The Hawkeye and ISEE 1 data provide some evidence for Z and O mode emissions at power levels typically about 20 dB or more weaker than the X mode AKR [Calvert, 1982]. High latitude Z mode signals are often detected by ISIS 1 [Muldrew, 1970; Benson, 1982a] and DE 1 [Gurnett et al., 1983]. The relative importance of the various modes and harmonics, in the framework of the cyclotron maser mechanism, has recently been addressed by Melrose et al. [1984]. They find that when spatial growth rate effects are considered that the Z mode becomes more important than the O mode - a prediction that is not supported by the results to be presented in the present paper.

The ISIS 1 correlative studies of AKR with the aurora [Benson and Akasofu, 1984] and inverted V electron precipitation [Benson and Calvert, 1979; Benson et al., 1980] supplemented and supported other satellite correlative studies involving AKR and the aurora [Gurnett, 1974], inverted V precipitation [Green et al., 1979] and field-aligned currents [Green et al., 1982]. Such investigations have been of particular significance because of the association of these phenomena with field-aligned electric fields which can give rise to the required electron distribution functions in the cyclotron maser mechanism of Wu and Lee [1979]. Such distribution functions have been measured by the S3-3 satellite [Mizera and Fennell, 1977] and have been incorporated into the cyclotron maser mechanism in several recent theoretical studies [Omidi and Gurnett, 1982; Wu et al., 1982; Dusenbery and Lyons, 1982; Omidi et al., 1984].

The ISIS 1 observations have also generated some controversies. The interpretation of the harmonic signals as natural phenomena [Benson, 1982a] has led to three different interpretations based on (1) a direct generation via the cyclotron maser mechanism [Wu and Qiu, 1983], (2) an instrument rather than natural origin [Calvert, 1983] and (3) a nonlinear process involving the coalescence of two cyclotron maser-produced Z mode waves [Melrose et al., 1984]. The present observations indicate that there are difficulties with each of these interpretations. The interpretation of AKR emissions below the X mode cutoff as O mode signals [Benson, 1984] has been recently challenged by Melrose et al. [1984] who claim that they are Z mode signals. The present observations will provide additional evidence to support the original interpretation while comparing X, O, Z and whistler (W) mode signals observed on ISIS 1 ionograms during high-altitude nighttime passes over the northern and southern auroral zones.

The objectives of the investigation are to classify the various high-latitude radiation phenomena observed on ISIS 1 topside ionograms in terms of ambient plasma parameters so as to make meaningful comparisons with the multitude of observational interpretations and theoretical predictions which have been proposed to account for various aspects of AKR. It is the result of applying a method used to study sounder-stimulated plasma resonances [Benson, 1982b] to the problem of characterizing naturally occurring noise signals, i.e., it combines the benefits of high frequency-resolution ISIS 1 sounder data with modern digital graphics techniques. The observations are presented in Sections 2-6, comparisons with theoretical predictions are made in Section 7 and the overall results are summarized in Section 8.

In Section 2 the frequency and intensity of the observed noise bands which are believed to be of natural origin are presented as a function of the ratio of plasma frequency f_N to electron cyclotron frequency f_H for the various propagation modes of the fundamental as well as the harmonic bands. Examples of some of these signals, which are classified into wave modes based on their frequency relationship to sounder-stimulated resonance and cutoff phenomena, are presented is Section 3. Detailed data inspections are made in Sections 4 and 5 in order to add support to the mode-classification technique and the claim that the harmonic signals are of natural (as opposed to instrumental) origin, respectively. Electron density contours along the satellite path from the satellite altitude down to the F layer peak are presented in Section 6 together with indicators of the recorded AKR intensities, the minimum altitude and the corresponding maximum (or quenching) f_N/f_H values for AKR generation. The implications of these observations to various AKR theoretical models are presented in Section 7 and a summary of the observations, theoretical implications and outstanding problems remaining is presented in Section 8.

2. Normalized AKR Frequencies vs. f_N/f_H

The distribution of the ISIS 1 data used in the present investigation in terms of altitude h, magnetic local time MLT and invariant latitude Λ is presented in Figure 1 and the corresponding dates and times for each of the 12 satellite passes investigated are presented in table 1. Also presented in Table 1 is information pertaining to the availability of cylindrical electrostatic probe (CEP) data used to provide high spatial resolution N_e information and references to figures containing ionogram illustrations and N_e contours for each pass. The restricted ranges of h, MLT and Λ in Figure 1 were selected so as to maximize the opportunity of encountering intense AKR; the selection being based on the results of an earlier statistical investigation using a much larger ISIS 1 data base (over 300 passes) [Fig. 5 of Benson and Calvert, 1979]. On each of the 226 ionograms investigated for natural noise bands, the ambient f_N/f_H value was determined from the sounder-stimulated resonance and cutoff phenomena [Benson, 1982b, and references therein]. These data, together with the frequencies and intensities of the observed noise bands, were recorded onto a data base for the highly flexible DEC PDP 11/70 graphics program developed for the investigation of stimulated resonances [Benson, 1982b]. The minimum and maximum frequency of each noise band was recorded and the corresponding signal intensity was classified into one of 3 levels: 1 for weak, 2 for moderate, 3 for strong (automatic gain control AGC voltage saturates) to intense (video signal saturates). The results of this analysis are presented in Figures 2-9.

Figure 2 presents the minimum frequencies normalized by f_H of all the AKR bands recorded as intensity 2 or 3, i.e., moderate to intense, and identified as either in the X, O or Z-mode. In this figure, the scaled frequencies for stimulated resonances, wave cutoffs and naturally occurring noise bands for a

single ionogram fall on a vertical line corresponding to the ionogram's f_N/f_H value. The horizontal dashes represent scaled or calculated values of the f_H, f_N and f_T (upper-hybrid) resonances and the electromagnetic Z and X wave cutoffs f_z and f_x, respectively, where

$$f_T^2 = f_N^2 + f_H^2$$

$$f_z = (f_H/2)\{-1 + (1 + 4\, f_N^2/f_H^2)^{1/2}\}$$

$$f_x = (f_H/2)\{1 + (1 + 4f_N^2/f_H^2)^{1/2}\} = f_z + f_H$$

(The f_z cutoff is given by X = 1 + Y in the notation of Ratcliffe [1959] and L = 0 in the notation of Stix [1962]; similarly, f_x is given by X = 1 - Y and R = 0.) In all cases, any calculated value was based on other observed features on the ionogram. For example, f_z may have been calculated from the scaled f_x. It is important to keep in mind that the f_N/f_H values plotted in Figure 2 (and in the following Figures 3-8) correspond to the value at the location of signal detection which does not necessarily coincide with the AKR source region. The main points to note in Figure 2 is that moderate to intense AKR is most often observed in the X-mode (which in turn is most often observed at low f_N/f_H values) and least often in the Z-mode. The O-mode, which represents an intermediate case, is observed even to large values ($\sim$1) of f_N/f_H.

Figure 3 presents similar results for the AKR bands recorded as intensity 1, i.e., weak. In this case noise bands identified as being in the whistler (W) mode appear below $f_H/2$ and at relatively large f_N/f_H values. Also, the Z-mode is very commonly observed, the X-mode is observed out to large f_N/f_H

values and the O-mode is now not as common at large f_N/f_H as it was in the data of Figure 2 which corresponded to stronger signals. The X's designating moderate to intense AKR in Figure 2 and weak AKR in Figure 3 when f_N/f_H is large correspond to remote sources, i.e., the indicated f_N/f_H values should not be considered to be source region values. Source region encounters correspond to low ambient values for f_N/f_H as will be illustrated in Figure 29.

Note that in both Figures 2 and 3 the X's, O's and Z's are near or above the wave cutoffs f_X, f_N and f_Z (designated by X, N and Z on the right borders of the figures), respectively. Indeed, these characteristics were used to help identify the various modes of propagation. (Frequencies observed slightly below wave cutoff are attributed to the 50 kHz receiver bandwidth.) In some cases the identification is not unique. For example, the Z's above the slanting f_N level could be O's, some of the O's below the slanting f_T level could be Z's (as has been argued by Melrose et al. [1984]) and even the X's could be O's (as has been argued by Oya and Morioka [1983]). The mode identification involves more than mearly the noise band minimum frequencies presented in Figures 2 and 3. The entire frequency extent of the signal must be considered (as will be discussed in connection with Figures 4, 5, 13 and 14), as well as the behavior of a given noise feature under changing plasma conditions (as will be discussed in connection with Figure 12) and the source region electron density structures (as will be discussed in Section 6). In addition, some of the data entries in Figure 3 (corresponding to weak AKR) corresponded to ionograms where the signal intensity increased above the weak level within the observed broadband fundamental AKR. For example, of the 69 X mode fundamental AKR entries in Figure 3 (which correspond to cases with weak signal strength at the minimum frequency end of the AKR band) 9 contained

frequency segments within the fundamental band that had intensity levels of 2 or 3. The majority of these cases occurred in the low f_N/f_H region ($f_N/f_H < 0.12$) near the X mode cutoff frequency ($f/f_H < 1.2$) - the region of greatest concentration of intensity 2 and 3 AKR in Figure 2.

The data of Figures 2 and 3 are separated further by intensities and wave modes in Figures 4 and 5 and displays of the entire frequency bandwidths of the noise bands are included. In addition, a collection of signals classified as "others" are presented in Figures 5c and 5f. Figure 4 displays (by intensity) the X and O mode minimum frequencies in the left column, the X mode minimum frequencies with the observed X mode signal bandwidths in the center column and the O mode minimum frequencies with the corresponding signal bandwidths in the right column. The display reveals information on the frequency component structure often observed with AKR. For example the single case of O mode AKR observed when $f_N/f_H \approx 0.8$ had a narrow band low frequency component of intensity 1 (Figure 4i) followed by a wide band intensity 3 component (Figure 4c). The "others" in Figures 5c and 5f are of two types: noise bands that could not be classified with confidence (minimum frequencies identified by asterisks) and noise bands associated either with the distributions of the upper hybrid frequency or the plasma frequency. Three of these signals related to f_N were observed with intensity 3; all other signals displayed in Figure 5 were either of intensity 1 or 2. These f_N signals may be the result of electrostatic noise generation in the medium. It is also possible that some of these signals, and those associated with f_T, could have been sounder induced, i.e., due to extremely long-duration stimulated plasma resonances. Even more likely is that some of these signals could be identified with one of the other designated propagation modes. For example, in Figure 5f it was a close call whether or not to designate the intensity 1

signal extending above f_N near f_N/f_H = 1.16 as O mode AKR and the 3 signals extending below f_N between f_N/f_H = 0.28 and 0.36 as W mode AKR.

A number of important features of AKR are apparent from Figures 4 and 5. Arranging the identified modes in the right two columns of Figure 4 and the middle column of Figure 5 in order of the highest maximum frequency to lowest maximum frequency yields the order X, O, Z, W (as will be discussed in connection with the histograms of Figure 14). In the right column of figure 4 the O mode minimum frequencies are seen to be less than the f_x cutoff (which implies that they are not in the X mode) and the O mode maximum frequencies often exceed f_T (which implies that they cannot be in the Z mode). An O mode example satisfying both of these frequency extremes will be presented in Figure 13. Of course, when the maximum frequency does not exceed f_T the signal could be in the Z mode as has been argued by Melrose et al. [1984]. The middle column of Figure 4 shows that the most intense X mode AKR is confined mainly to the lowest f_N/f_H values sampled and X mode AKR is observed to higher values of f_N/f_H as the signal intensity decreases. A comparison of Figures 4b and 4c reveals that intensity 3 AKR is observed much more frequently in the X mode than in the O mode whereas a similar comparison of Figures 4e and 4f reveals that intensity 2 AKR observed under conditions of large f_N/f_H is dominated by the O mode. The middle column of Figure 5 shows that Z mode AKR is most often observed to be a weak signal (intensity 1), that it is sometimes well confined between f_N and f_H (as will be discussed in Section 3 in connection with the ionogram examples of Figure 11) and that the Z mode minimum frequency is in general not constrained by f_N - which adds support to the mode identification as Z rather than O (as will be discussed in connection with the ionogram examples of Figure 12). At the higher altitudes of the DE-1 satellite only the Z mode signals confined between f_N and f_H are

observed [Gurnett et al., 1983]. The W mode peak frequency is observed to be bounded by $f_H/2$ (Figure 5e) which suggests that the W mode signals are ducted to the spacecraft as will be discussed in Section 7.

The X and O mode data of Figures 2, 3 and 4 are repeated in Figures 6, 7 and 8 with the addition of the harmonic noise bands observed by ISIS 1. The Z and W mode data are not repeated because no harmonics have been observed to be associated with these modes. The main points to note concerning the X mode harmonic AKR observations are the following: High order ($\geq 3^{rd}$) X mode harmonics of moderate intensity are observed only for the minimum values of f_N/f_H sampled (~0.1) (Figure 8e), whereas the corresponding weaker harmonics can be observed to higher f_N/f_H values (Figure 8h). X mode harmonics have been identified out to the 4^{th} (the harmonic off-scale near $f_N/f_H = 0.1$ on Figures 8g and 8h is a 4^{th} harmonic with a large separation from 4 f_H). The minimum frequencies of the X mode 2^{nd} harmonics increases with increasing f_N/f_H but not as fast as twice the X mode fundamental which is bound by the rising f_x cutoff (Figures 8e and 8h). (This observation will be even more apparent from Figure 21 where harmonic signals from the same ionogram will be compared.)

Since the O mode harmonics of Figures 6, 7 and 8 are observed to occur at frequencies above f_x, i.e., above the slanting f_x cutoff line designated by X in each frame, they could be X mode signals. They are here identified as O mode harmonics for the reason cited earlier [Benson, 1984], i.e., they are observed to be associated with what is here identified as O mode fundamental AKR. These harmonics are observed predominantely below $2f_H$ when f_x is near f_H (small f_N/f_H) and above $2f_H$ when f_x is much larger than f_H (large f_N/f_H) (see Figures 8f and 8i). An illustration comparing O and X 2nd harmonic noise bands under conditions of low f_N/f_H will be presented in Figure 32 and the overall distribution of X and O mode 2nd harmonics relative to $2f_H$ will be

presented in Figure 33. Ordinary mode harmonics have been observed out to the 3rd (those straddling the $4f_H$ line near f_N/f_H = 1.0 in Figure 8i are 3rd harmonics with large separations from $3f_H$).

The number of ionograms corresponding to the X, O, Z and W entries of Figures 5a, 5d, 8a, 8d and 8g are indicated in histogram-form in Figure 9. From Figure 9a it is seen that over 1/3 of all the ionograms recorded under ambient conditions with $f_N/f_H < 0.2$ had intensity 3 fundamental X mode AKR (designated by XM1 in Figure 9). Adding the XM1 totals from Figures 9b and 9c indicates that 88% of all ionograms recorded under such auroral zone plasma conditions detected fundamental X mode AKR. The corresponding figures for the 2nd, 3rd and 4th X mode harmonics (designated in Figure 9 by XM2, XM3 and XM4, respectively) are 77%, 37% and 4%, respectively.

The O mode distributions in Figures 9d and 9e are undoubtably influenced by the overwhelming presence of the dominant X mode AKR since, as already mentioned, the data were selected primarily based on earlier AKR X mode observations (see also the discussion relative to Figures 17 and 18). Weak Z mode AKR is observed under all f_N/f_H conditions whereas W mode signals are observed only for relatively large f_N/f_H (Figures 9f and 9g). The restriction in the W mode distribution is due to instrumental limitations, i.e., since the W mode is confined to the frequency range below the smaller of f_N and f_H it cannot be observed in the main AKR density cavity when $f_N < 0.1$ MHz (the ISIS 1 swept frequency receiver lower cutoff).

Ionogram examples illustrating some of the data displayed in figures 2-9 will be presented in the next section.

3. Ionogram Examples

A large number of ionogram reproductions illustrating X mode AKR, with harmonics, have been published [Benson and Calvert, 1979; Benson et al., 1980;

Benson, 1982a; Benson and Akasofu, 1984]. Examples of O mode AKR, with harmonics, have been presented by Benson [1984]; some of these illustrations also contained W mode AKR, e.g., see the signals with $f < f_N < f_H$ in Figure 3 and those with $f < f_H/2 < f_N = f_H$ in Figure 4 of Benson [1984]. The W mode signals detected in the present high altitlude data set were all of low intensity. ISIS 1 high-latitude ionograms recorded at lower altitudes reveal more intense W mode signals (e.g., see Figure 5 of Muldrew [1970] and Figure 2 of Benson [1981]). ISIS 1 examples of high latitude Z mode radiation have also been presented (see again Figure 5 of Muldrew [1970]; also Figure 8 of Benson [1982a]).

It has been suggested by Melrose et al [1984] that the AKR examples identified as O mode in Benson [1984] could be Z mode signals. Ionogram examples will be presented in this section to support the mode identification used here and in Benson [1984]. (Further evidence in this regard will be presented in the next section in connection with Figure 14).

Figure 10 presents an ISIS 1 example illustrating Z mode AKR (ZM), fundamental O mode AKR (OM1) and 2nd harmonic O mode AKR (OM2). The latter signal could also be X mode but is here identified as O mode because of its harmonic relationship to OM1. Note that ZM extends approximately from f_N to f_T and that OM1 starts with $f < f_x$.

Figure 11 presents a sequence of ISIS 1 ionograms which are included here (even though they are not from the present data set, i.e., not one of the 12 passes represented in Figure 1) because they reveal strong signals well confined between f_N and f_H which are present even during an interval when the sounder transmitter was off (part of the fixed frequency portion and all of the swept frequency portion of ionogram c). Thus these signals are definitely of natural origin rather than being sounder-induced. They have a similar

appearance to the Z mode signals observed on cusp region ionograms as reported earlier by James [1976]. Based strictly on the data reproduced in Figure 11 it would be difficult to determine whether these signals are in the Z or O mode because both modes can propagate in the frequency range between f_N and f_H when $f_N < f_H$. Such noise bands are observed to persist, however, even when the ambient electron density increases to the point that f_N exceeds the noise band minimum frequency. An example of such a condition, which implies that the noise signal is in the Z mode, is presented in Figure 12.

Figure 12 presents a sequence of 8 consecutive ionograms when the ISIS 1 sounder was operating in a 2-on/2-off mode, i.e., the sounder transmitter was on for 2 ionograms and then off for 2 ionograms (with the receiver on). The sounder transmitter was on during ionograms c, d, g and h and off during ionograms a, b, e and f. During the transmitter-off ionograms the noise near 0.5 MHz can definitely be established to be of natural origin. The modulated appearance of the intense signals from about 1.3 to 1.6 MHz indicate that they are due to signals transmitted from medium-frequency broadcast stations which can break through the ionosphere under certain conditions [see the discussion with Fig. 18 of Hagg et al., 1969]. The higher frequency signals are also attributed to interference from ground stations even though some of them may be at frequencies less than the ionospheric critical frequency beneath the satellite [Hagg et al, 1969].

The natural noise between about 0.25 and 0.6 MHz in Figure 12 is attributed to Z mode AKR with superimposed intense narrow-band electrostatic noise at f_N on ionograms b, f and g. The wide-band noise is attributed to Z mode rather than O mode signals because the plasma frequency (as indicated by the sounder-stimulated f_N resonance) can be well inside the noise band (Figure 12h) as well as at the low frequency edge (Figures 12c and 12d). This

location of f_N can also be determined from the sporatic f_N electrostatic narrow-band signals in Figures 12b and 12f and (superimposed on the f_N resonance) in Figure 12g.

The wide-band Z mode noise is sampled for a little over 3 seconds during the fixed frequency (0.48 MHz) portion of each ionogram in Figure 12. The uniformity of the darkness of the noise signal and the lack of significant fluctuations in the level of the AGC signal (white trace near 28 msec time delay) on each of these ionograms indicates that the Z mode AKR during this event was fairly continuous over time intervals of several seconds. Furthermore, the continuity of signal level between adjacent ionograms in Figure 12 suggests that the Z mode AKR was fairly steady over time intervals of 10's of seconds.

As with the case of Figure 11, the data presented in Figure 12 are not from the data set represented in Figure 1. They are presented here for the following reasons: (1) they clearly indicate the natural origin of both narrowband signals associated with f_N (presumably electrostatic) and wide-band signals attributed to the Z mode during observing periods with the sounder-transmitter off, (2) they illustrate the time-continuity of the signals because of the fortuitous coincidence of the chosen value for fixed frequency operation and the frequency interval containing Z mode signals and (3) they illustrate the transition of f_N through a Z mode signal that remains relatively stable in the frequency domain. This last point is characterized in the present data set by the Z mode minimum frequencies that can be observed below as well as above f_N (see Figures 5d and 5e).

Figure 13 presents an example of an AKR signal which is interpreted in terms of cold plasma dispersion theory as O mode because the minimum frequency is less than f_x (thus it is not X mode) and the maximum frequency is greater than f_T (thus it is not Z mode) even after allowing for the effect of the

receiver bandwidth. Such examples are difficult to find because when the ambient N_e becomes much lower f_x approaches so close to f_H that it is difficult to identify the AKR minimum frequency below f_x and when N_e becomes much higher f_T approaches the O mode AKR maximum frequency. In addition, X mode AKR (which can mask the O mode AKR maximum frequency) is often simultaneously observed. When warm plasma dispersion effects are considered for small f_N/f_H, the AKR X mode frequency can be considerably less than the cold plasma cutoff f_x [Wong et al., 1982]. The effect such warm plasma dispersion corrections may have on the interpretation of the present data will be discussed in Section 7.

4. A closer look: wave modes

The data presented in Section 2 will be displayed in this section in different formats in order to investigate the maximum frequencies of the various modes and the data distributions in terms of Λ, MLT and h.

Figure 14 presents the maximum frequency of each of the fundamental AKR modes observed. As pointed out pertaining to the discussion of Figures 4 and 5 in Section 2, it is readily apparent that the maximum frequencies are greatest for the X mode followed (in order) by the O, Z and W modes. The only unobscured maximum frequencies in this figure correspond to the X and W modes since the O mode is often obscured by the X mode and the Z mode by the O mode. The W mode cutoff corresponds to $f_H/2$ as mentioned in Section 2.

The intensity 1 XM1 data are presented separately in Figure 14a because they are so weak it is often difficult to classify them with confidence as an AKR signal rather than as an "other". Some of these weak "others" (see Figure 5f) occupy essentially the same frequency domain as the higher frequency components of weak X mode AKR (see Figure 4h). The classification into X mode AKR is usually based on the trend established over a series of ionograms

containing AKR, whereas the classification as an "other" may be based on the absence of such a trend and/or to the presence of a different appearance to the signal modulation. This different appearance may result from ionospheric break-through of man-made signals from the ground as discussed in the last section in connection with the much stronger signals of Figure 12.

Even though the O mode distribution of maximum frequencies in Figure 14b is often limited by the obscuring effect of a more dominant X mode, it is fairly steady out to the sharp drop at 680 kHz. This limit is the same as the main drop in the distribution of the maximum frequencies of the intensity 2 and 3 X mode signals (Figure 14a). Since these maximum frequencies provide an indication of the minimum altitude of AKR generation [Benson and Calvert, 1979], the minimum source region altitude for the 2 modes should be somewhat similar. This result is supported by individual case studies in section 6. The Z mode cutoff frequency is considerably lower than that of the X or O modes. The distribution of maximum frequencies falls off sharply just above 500 kHz (Figure 14c); this behavior is the result of the constraint $f < f_T$ for the Z mode and the obscuring effect of the O mode. The similarity in the maximum frequencies observed for the X and O modes (neither of which are restricted from propagating in free-space) and the considerably lower values observed for the case of the Z mode (which is so restricted) adds a degree of confidence to the present mode classification.

Figures 15 and 16 present the distribution of the ambient f_N/f_H values against Λ for the various modes by signal intensity. It is seen that intensity 3 AKR is mainly limited to the X mode in the 62 to 75° Λ range (Figure 15, top), intensity 2 AKR at low latitudes is dominated by the O mode (Figure 15, middle) and intensity 1 AKR is observed throughout the data set on all modes (bottom frames in Figures 15 and 16) - except for the W mode which is restricted by instrumental effects as mentioned in Section 2.

The data distributions in Λ, MLT and h are presented in histogram-form for the X mode (including harmonics) in Figure 17, the O mode (including harmonics) in Figure 18 and the Z and W modes in Figure 19. Since the data for this study were selected mainly from the point of view of obtaining a good sample of strong to intense fundamental X mode AKR, it is not surprising that the resulting distribution of intensity 3 XM1 in Λ in Figure 17a is very consistent with the earlier results of Benson and Calvert [1979]. The O and W modes are limited by a lack of more low altitude (and hence higher N_e) data (Figures 18a and 19d). The Z mode is observed at all Λ sampled (Figure 19d) as well as at all MLT and h (Figures 19e and 19f).

The main features of the X and O mode distributions of Figures 17 and 18 are the following: (1) Intensity 3 XM1 is restricted to limited ranges of Λ, MLT and h (Figures 17a, 17b and 17c) but intensity 1 XM1 is observed over nearly the full extent of the available data set in these parameters (Figures 17g, 17h and 17i). (2) Intensity 2 XM2 extends over nearly the same ranges in Λ, MLT and h as intensity 2 XM1 (Figures 17d, 17e and 17f) and intensity 3 XM1 (Figures 17a, 17b and 17c). (3) The higher harmonics, on the other hand, are restricted in Λ and MLT; Intensity 2 XM3 and XM4 and intensity 1 XM4 are restricted to 65 to 75° Λ (Figures 17d and 17g) and to 20 to 21 and 00 to 01 LMT (Figures 17e and 17h). (4) OM2 extends over about the same range in Λ, MLT and h as does OM1 (Figure 18). (5) Intensity 1 OM3 and intensity 2 OM2 are not restricted in Λ or h (Figures 18a, 18c, 18d and 18f) but they are restricted in time to the ranges 20-22 and 01-03 MLT (Figures 18b and 18e).

The significance of highlighting the distributions of the higher harmonics is that they provide information on the location of the AKR source regions [Benson and Calvert, 1979]. This matter will be discussed further in Section 6 in connection with Figure 29.

5. A closer look: harmonics

The harmonic emissions represent one of the most puzzling problems of the AKR phenomenon to explain. The interpretation that they are real [Benson, 1982a] and even exist in the O mode [Benson, 1984] has recently been challenged by Calvert [1983] who favors an instrumental origin. A resolution of this controversy takes on added importance in view of the recent theoretical efforts to account for the observations [Wu and Qiu, 1983; Melrose et al., 1984].

In Section 2 the AKR data from all 12 ISIS 1 passes were presented as a single ensemble which, in general, made it impossible to determine which set of harmonics belonged to the same ionogram, e.g., a particular XM3 could not be compared to the corresponding MX2 and XM1 signals. In the present section, fundamental and harmonic signals from the same ionogram are compared. The data from each of the 12 passes of Figure 1 were presented in pass plots such as the one displayed in Figure 20. The pass presented in Figure 20 contains 32 ionograms. On each of these the scaled f_H and nf_H values (with n up to 4) are displayed as horizontal bars while the scaled AKR bands are displayed as vertical bars of a length representing the observed bandwidth and a thickness proportional to the observed signal intensity. From this presentation, frequency ratios were calculated for the ionograms containing X mode fundamental AKR plus one or more harmonics, e.g., on a given vertical line representing a single ionogram, the maximum frequency of an XM2 bar would be compared with the maximum frequency of an XM1 bar. Similar measurements were made for the 11 other passes. The combined results of all the frequency ratios, each from a single ionogram, are presented in Figure 21.

The purpose of the Figure 21 presentation is to determine if the harmonic noise bands are exact multiples of the fundamental AKR band since such an

exact relationship would be an indication of a possible instrumental origin for the harmonics [Benson and Calvert, 1979]. The results presented in Figure 21a indicate that the maximum frequency of the 2nd harmonic XM2(max) is more often less than twice the maximum frequency of the fundamental XM1(max) for both the total distribution and for a distribution based only on ratios involving intensity 3 XM1. Similar results are obtained when only ratios involving intensity 2 or 1 XM1 are considered (Figures 21b and 21c).

When the minimum frequencies of XM2 and XM1 are compared, the signals are much closer to being harmonically related. It is found that there are slightly more cases with XM2(min) > 2[XM1(min)] when only intensity 3 XM1 are considered (Figure 21d) but the situation reverses when only lower intensity XM1 are considered (Figures 21e and 21f). In fact, a comparison of Figures 21e and 21f indicates that the number of cases with XM2(min) < 2[XM1(min)] increases as the signal intensity of XM1 decreases. These observations, based on comparisons of harmonic and fundamental signals on individual ionograms, are consistent with the ensamble presentation for large f_N/f_H in Figure 8h.

A similar analysis comparing XM3 and XM1 minimum and maximum frequencies indicates that XM3(max) is always less than 3[XM1(max)] (Figures 21g and 21h) whereas XM3(min) is more often greater than 3[XM1(min)] (Figures 21i and 21j). This unexpected reversal in the trends between ratios involving minimum and maximum frequencies of XM3 suggests that the XM3 generation mechanism may not be as similar to that of XM2 as previously thought. It also indicates that the bandwidth of XM3 must be considerably less than three times the bandwidth of XM1.

The bandwidths of the XM1 through XM4 modes are presented in Figure 22. The bandwidth of XM1 is limited on the low frequency side by the cutoff frequency f_x which must be greater than f_H (see Figure 23) and by the maximum

generation frequency of the fundamental X mode AKR signal (see Figure 14a) which is presumably determined by the quenching of the generation mechanism in the higher density region well below the satellite.

In Figure 24 the AKR X mode bandwidth ratios between the 2nd harmonic and the fundamental and the 3rd harmonic and the fundamental (each ratio being determined from the same ionogram) are presented. It is clear from this figure that the bandwidths of the harmonic AKR bands are less than the corresponding multiples of the fundamental bandwidth.

Thus the conclusions inferred from the presentations of Figures 21 and 24 are that the X mode AKR harmonic bands are not exact frequency multiples of the fundamental, which in turn implies that the harmonics are not caused by a nonlinear receiver response to an intense wide band signal.

Calvert [1983] has recently suggested that the AKR harmonics are the result of a nonliner receiver response to intense monochromatic signals resulting from a feedback mechanism operating in the AKR source region [Calvert, 1982]. He claims that the observed AKR bandwidth is merely a reflection of the receiver bandwidth which increases substantially for very strong signals. The observed AKR bandwidths do not support this view because the distributions do not indicate any particular favored bandwidth that could be identified with an expanded receiver bandwidth (Figure 22), the AKR harmonic bandwidths do not change significantly as a function of signal intensity (e.g., compare Figures 22c and 22d) and the AKR 2nd harmonic bandwidth is more often greater than that of the fundamental whereas the 3rd harmonic bandwidth is observed to be less than the fundamental bandwidth just about as often as it is observed to be greater (Figure 24).

Calvert [1983] also argued that the observations that the 2nd harmonic is sometimes greater than the fundamental [Benson, 1982a] could be explained by

variations of the incoming fundamental signal during the sweep between the fundamental and harmonic frequencies as originally proposed by Benson and Calvert [1979]. While it is true that a great variability in AKR signal intensity on a milisecond time-scale can be observed on ISIS 1 ionogrms (see e.g., the spotty appearance of the OM1 and OM2 signals along the time delay axis in Figure 10) the overall signal level often remains intense for periods of 10's of seconds as indicated by the ocassions when the sounder receiver fixed frequency coincides with the frequency of an AKR band (see, e.g., the examples of Figure 1 of James [1980] and Figures 2 and 4 of Benson and Akasofu [1984]). Under these conditions the main signal variations are usually caused by the nulls in the radiation pattern of the spinning ISIS 1 dipole. Indeed, it was this very AKR characteristic, i.e., a signal intensity steady and strong enough so as to saturate the ISIS 1 receiver's AGC voltage for time intervals long compared to the time interval between antenna spin nulls (~ 10 sec), that enabled James [1980] to make AKR direction-of-arrival measurements. In addition, it is possible to find cases where several consecutive ionograms have a 2nd harmonic AKR signal more intense than the fundamental. An example is presented in Figure 25. Here the first 5 of 6 consecutive ionograms contain 2nd harmonic AKR with greater signal intensity than the fundamental; the two signals are of comparable intensity on the last ionogram. It is unlikely that the AKR signal variations could be syncronized with the satellite spin period over a time interval of 2 minutes to produce such an effect.

Benson [1982a] also indicated that at times the AKR harmonic signal corresponds to the weaker of two frequency components on the fundamental AKR band (e.g., see Figure 6 of Benson [1982a]) and that distinct frequency components of high signal intensity can be observed on the fundamental but not

on the harmonics (e.g., see Figure 5 of Benson [1982a]). This latter example corresponds to the data labelled "b" in Figure 20a and to the portion of ionogram b in Figure 26. The ionogram strips on the right side of Figure 26 are from the same ISIS 1 pass used to obtain Figure 20 and they correspond to the scaled data labeled a-g in Figure 20a. Also shown in Figure 26 are the energetic electron data from the ISIS 1 soft particle spectrometer which indicate that the satellite encountered a wide double inverted V structure - with a component on each side of ionogram e. If the AKR frequency component structure evident on ionograms b, c, d, f and g in Figures 20a and 26 is assumed to be due to a double source structure, then the component closest to f_H would be attributed to the local source and the component with the large frequency gap to the more distant source [Benson and Calvert, 1979; Calvert 1981a]. The continuity of the fundamental AKR signal between ionograms b and f suggests that the double inverted V structure displayed on the left side of Figure 26 is a spatial rather than a temporal feature. Such continuity of spatial features has also been suggested in the Dynamics Explorer data [Hoffman and Lin, 1981; see also the review article by Lin and Hoffman, 1982]. The relevance of this discussion to the harmonic question is that the AKR 2nd harmonic in Figure 26 always corresponds to the fundamental AKR component corresponding to the local source even when the remote frequency component of the fundamental is stronger than the local component as it is on the two consecutive ionograms f and g in Figure 26 (this intensity feature is easiest to see from the scaled data displayed in Figure 20a).

Thus the observations displayed in Figures 25 and 26 argue against the interpretation that examples of 2nd harmonic AKR signal strengths greater than the fundamental are caused by time variabilities of the source. Another argument against such an interpretation is that one would then expect the 3rd

or 4th AKR harmonics to occasionally be observed with signal intensities stronger than a lower harmonic or the fundamental. While 24 of the 129 observed XM2 AKR bands were observed with intensities greater than XM1, i.e., 1 in 5, none of the 43 XM3 or 6 XM4 AKR bands were observed with intensities greater than a lower order signal. If source variability was the cause of the above 24 strong XM2 signals, and if the same variability was present when the XM3's and XM4's were recorded, then at least 8 XM3 and one of the XM4 signals should have been observed with signal intensities greater than a lower order signal. The numbers become even more impressive against the variability hypothesis when one considers that all the cases of moderate and weak harmonics corresponding to moderate and weak fundamentals (e.g. see Figures 3 and 4 of [Benson 1982a]), would have to be explained in the same manner.

6. Source Region N_e Structures

The source region N_e structure is of fundamental importance to AKR theories. The cornerstone of the Wu and Lee [1979] doppler shifted cyclotron mechanism was the AKR source region ISIS 1 N_e cavity observations of Benson and Calvert [1979]. The mode-conversion theories of Oya and Morioka [1983] and Jones et al. [1984] require sharp N_e boundaries and large density enhancements (several orders of magnitude), respectively. The feedback mechanism of Calvert [1982] requires density enhancements of the order of 20%.

The ISIS 1 topside sounder provides unique data in this regard. In addition to providing in-situ N_e values, it also provides vertical N_e profiles below the satellite. These profiles enable the minimum altitude of the AKR source region and the corresponding $(f_N/f_H)_{max}$ value to be determined [Benson and Calvert, 1979]. The profiles can be combined to produce N_e contours through the AKR source region from the satellite altitude to the altitude of the F layer ionization peak density [Benson et al., 1980]. Such contours,

using a curved earth format, have been presented for 5 of the 12 passes represented in Figure 1 by Benson and Akasofu [1984]. The contours for the other 7 passes are presented in Figures 27 and 28. References to the 12 contour presentations are given in Table 1.

Figure 27 presents the sounder-derived N_e contours for the ISIS 1 data presented in Figures 20 and 26 in the bottom, and high spatial resolution data inserts from the ISIS 1 cylindrical electrostatic probe CEP at the top. Since N_e is linearly proportional to the probe current, the CEP data clearly reveal that the maximum N_e enhancements between ionograms recorded from within the AKR density cavity (N_e <100cm^{-3}) were of the order of a factor of 3 (compare the 2-sec probe sweeps on the right side with those on the left side of the CEP data in the lower of the two CEP data inserts, i.e. corresponding to the interval between ionograms b and c). Sudden N_e variations of the order of several 10's of percent were observed within individual 2-sec probe sweeps. For example, see the approximately 20% enhancement near the end of the first 2-sec sweep in the above mentioned CEP data. This particular enhancement takes place within the spacing of two CEP data points (collected at the rate of 120 samples/sec) corresponding to a motion of the satellite of only 1/10 km. Such sharp density gradients are 10 times greater than those required in the feedback model of Calvert [1983]. It is difficult to say, however, whether enhancements of this type would have the required transverse dimensions of about 20 km (see Figure 8 of Calvert [1983]) since such distances would in general involve two consecutive 2-sec CEP sweeps. Under conditions of low N_e the CEP curves are sometimes superimposed on one another, and sometimes some data sweeps are not plotted due to software limitations, so that comparisons from one curve to another is often difficult.

In Figure 27 the AKR source encounters are indicated by the magnetic field line projections extending down from the AKR intensity symbol marking the satellite location to the X (designating X mode AKR). The heavy portion of this field-line projection indicates the extent of the region of AKR generation below the satellite. This source projection is based on the observed maximum frequency of the AKR fundamental frequency [Benson and Calvert, 1979]. The two horizontal bars on each of these bold portions of the field-line projections indicates the estimated uncertainties in this technique for this series of ionograms. The selection of source encounters was based on the closure of the frequency gap between the AKR fundamental band and f_H [Benson and Calvert, 1979], with the added constraint that the frequency gap between the AKR 2nd harmonic and $2f_H$ [Benson and Akasofu, 1984] also be closed. The AKR symbols indicate that strong to intense AKR was observed throughout most of the AKR density cavity. These observations are very typical of high altitude passes through an extended AKR density cavity as pointed out by Benson and Akasofu [1984] (see, e.g., Figure 4 of that study).

The N_e contours in Figure 27 are based on sounder-derived vertical N_e profiles beneath every satellite position indicated by an AKR intensity symbol. These profiles are based on the assumption of a horizontially stratified ionosphere [e.g., see Jackson, 1969] and some caution must be used in interpreting the results far below the satellite in regions of extreme latitudinal gradients such as those shown on the right side of Figure 27. Added confidence in the detection of such gradients, however, is obtained by comparing the sounder and CEP results. The increase in N_e far below the satellite between ionograms b and c as deduced from the sounder-derived profiles is also detected in situ by the CEP. Similarly, the remote N_e variations between the satellite positions where the 10^2 and 3×10^2 N_e

contours are encountered are also detected by the CEP, i.e., an increase in N_e which levels off and then increases again (see the top CEP insert of Figure 27).

Figure 28 presents N_e contours, AKR source field lines with the extent of the source region indicated by the bold portions, the AKR intensity symbols and the inferred AKR propogation mode (at the top and bottom of each source field line, respectively) for 6 of the 12 passes of Table 1. From an inspection of the data in Figures 27 and 28 and Figures 3-7 of Benson and Akasofu [1984], it can be seen that the AKR density cavities ($N_e < 100$ cm^{-3}) range from a few degrees to more than 20° in latitude and that the minimum altitudes for X and O mode AKR generation are similar and that they range from 2300 to 3300 km (the average was found to be 2700 km).

The X mode source encounters indicated in Figures 27 and 28 and from Figures 3-7 of Benson and Akasofu [1984] were used to create a data subset. The resulting distributions in f_N/f_H, MLT, Λ and h are presented in Figure 29. Even though the X mode source encounters with an intensity 3 fundamental are observed to be restricted in the above parameters, a comparison with Figures 9a, 9b, 9c and 17 indicates that they are generally not as restricted as the cases where higher X mode harmonics of lower signal intensity are observed. This comparison is particularly striking in the case of the parameter Λ. Figure 29c indicates that intensity 3 X mode source encounters were observed from 55 to 75° Λ whereas X mode moderate intensity 3rd and 4th harmonics (see Figure 17d) and weak 4th harmonics (see Figure 17g) were only observed between 65 and 75° Λ.

7. Data/theory comparisons

The present data will be compared mainly with two mechanisms for the generation of AKR: (1) the doppler-shifted cyclotron theory originally

proposed by Melrose [1976] and modified by Wu and Lee [1979] to agree with energetic auroral zone electron observations and (2) the Z to O wave mode-conversion models of Oya and Morioka [1983], Jones [1977], and Jones et al. [1984]. The reasons for concentrating on these two mechanisms are the following: numerous theoretical calculations, which predict AKR intensity levels for various propagation modes and harmonics as a function of the source region f_N/f_H (from $<<$ 1 to $\approx$ 1), have been performed on the first mechanism and the second mechanism requires sharp gradients in N_e in the vicinity of the AKR source region. The ISIS 1 AKR source region measurements, which include remote as well as ambient N_e information, are uniquely suited for investigating these mechanisms. For a theoretical review that includes additional mechanisms, see Grabbe [1981]. Recent work since the publication of this review include the linear electrostatic-to-X mode electromagnetic wave conversion mechanism of Istomin and Pokhotelov [1983], the mechanism of Bujarbarua and Nambu [1983] based on an induced bremsstrahlung interaction between aurora beam electrons and double layer potentials which has been recently modified by Bujarbarua et al. [1984], and a lively discussion [Maggs and Roux, 1983; Grabbe, 1983] of the nonlinear wave-wave interaction mechanism of Grabbe et al. [1980]. There have also been a large number of recent theoretical studies concerning mechanism (1) which is basically a cyclotron maser process [Wu, 1981; Wu et al., 1981a, 1981b; Melrose et al., 1982; Omidi and Gurnett 1982; Wu et al., 1982; Wong et al., 1982; Dusenbery and Lyons 1982, 1983; Hewitt et al., 1982; Wagner et al., 1983, 1984; Freund et al., 1983; Hewitt and Melrose, 1983; Hewitt et al., 1983; Wu and Qiu, 1983; Wong, 1983; Le Queau et al., 1984a, 1984b; Omidi et al., 1984; Melrose et al., 1984; Lyons and Dusenbery, 1984; Pritchett, 1984] and a major new twist involving a feedback mechanism in the generation region has been proposed by Calvert

[1982]. Mechanism (2) is the outgrowth of a process originally applied to Jovian decametric radiation [Oya, 1974] and later applied to AKR [Benson, 1975].

Instability growth rates: X, O, Z and W modes

A major emphasis in most of the theoretical studies involving the first mechanism has been directed toward the calculations of linear instability temporal growth rates. These calculations are extremely sensitive to the source region f_N/f_H value. The maximum inferred values for f_N/f_H, corresponding to the minimum source region altitude for the source encounters indicated on Figures 27 and 28 and Figures 3-7 of Benson and Akasofu [1984], were obtained for both the X and the O modes using the methods of Benson and Calvert [1979] (for X) and Benson and Akasofu [1984] (for O). The results are presented in Figure 30 together with the calculated maximum temporal growth rates of Melrose et al. [1984] for the fundamental and 2nd harmonic X and O modes and the fundamental Z mode. The sharp drop in the X mode growth rate with increasing $f_N/f_H = \omega_p/\Omega_e$ until it is no longer the dominate mode, which is so apparent in Figure 30 when f_N/f_H is between 0.2 and 0.3, was first pointed out by Lee et al. [1980] in a comparison of maximum temporal growth rates of the X and O modes; it has been illustrated more recently in a comparison of maximum growth rates of the fundamental and 2nd harmonic X mode emissions by Wu and Qiu [1983] and in the numerical simulations of Wagner et al. [1984]. Excellent agreement is found between the values deduced from the observations for the fundamental X and O modes and the predicted ones corresponding to the highest growth rates - especially since there were some mode-identification uncertainties associated with the 3 X mode entries with $f_N/f_H > 0.25$, i.e., they may be O mode rather than X mode. Similar comparisons were not made for the Z mode because the location of the source region in this case is uncertain.

While the data theory agreement displayed in Figure 30 appears to be very favorable, it may not represent the most meaningful comparison since it is based strictly on temporal growth rates. Indeed, Melrose et al. [1984] argue that the Z mode, rather than the O mode, should dominate when $0.3 \lesssim f_N/f_H \lesssim 1.3$ (with a signal intensity comparable to the most intense X mode at the lower end of this range) due to spatial growth rate effects if the maser action does not saturate. They further argue that it is unlikely that the O mode or 2nd harmonic X mode are produced directly by the maser process. They suggest that the former is produced by mode-conversion from an X mode incident on a sharp N_e boundary and that the latter is produced by the coalescence of two Z mode waves. There are observational difficulties with these suggestions, however, because the Z mode is never observed with signal levels comparable to the most intense X mode, the O mode is observed without an accompanying X mode when $f_N/f_H \approx 1$ (compare Figures 4e and 4f), the O mode is observed more often with a greater intensity than the Z mode (compare OM1 and ZM in Figures 9d and 9f) and the most intense 2nd harmonic X mode is observed under ambient conditions of $f_N/f_H < 0.2$ (see XM2 in Figure 9a) whereas the predicted Z mode dominance is for $f_N/f_H \gtrsim 0.3$.

The relative signal intensity between different modes is sometimes difficult to quantify from ISIS 1 data in the ionogram format. Figure 10 illustrates a case where the O mode signal (OM1) is more intense than the neighboring Z mode signal (ZM). Unfortunately, there is no AGC trace present on this ionogram (a condition which existed on 1/2 of the ionograms used in the present investigation). Cases can also be found where the Z mode signal intensity is greater than the O mode intensity. In general, however, the O mode signals are stronger - by about 5dB based on AGC calibration curves. In each case the peak signal levels are near the point of AGC saturation - a

level commonly exceeded by the fundamental X mode AKR. This AGC saturation level of ISIS 1 occurs at the relatively low signal of 65dB below a 1mW cw input power level, i.e., at -65dBm. From this level the receiver has nearly 60dB of dynamic range before the video signal output is saturated (corresponding to a signal input of -6dBm). An inspection of sounder-receiver video amplitude records reveals that intense X mode AKR can reach power levels corresponding to -30dBm. Comparing representative intense AKR power levels indicates that intense X mode signals are approximately 30 to 35dB stronger than intense O and Z mode signals, respectively. These relative X to Z mode signal levels observed by ISIS 1 in the lower portion of the AKR source region are in agreement with the relative intensities between X mode AKR and Z mode radiation observed at much higher altitudes over the auroral regions by DE 1 [Gurnett et al., 1983]. Thus there is no observational evidence that the Z mode can be of comparable intensity to the X mode as claimed by Melrose et al. [1984].

Melrose et al. [1984] cautioned that their results are specifically for one-sided loss cone electron distribution functions. When the distribution function includes a beam feature for the downgoing electrons, and a ring feature in the transverse direction, the relative growth rates can be considerably different as can be seen from the work of Freund et al. [1983]. They show, for example, that under such conditions the maximum temporal growth rate of the 2nd harmonic X mode is nearly comparable to that of the fundamental O mode when $f_N/f_H = 0.5$ to 0.7 rather than the one order of magnitude gap between these emissions as indicated by the work of Melrose et al. [1984] (see Figure 30). The work of Omidi et al. [1984], which also employs an electron distribution function that allows for free energy sources other than the loss cone feature, indicates that Z mode AKR is generated in the frequency region

below f_H. The growth of Z mode waves in the work of Hewitt et al. [1983] and Melrose et al. [1984], on the other hand, is confined to the frequency region above f_H and special propagation conditions must be invoked to account for the Z mode signals observed below f_H by Gurnett et al. [1983] and many of those observed in the present work (see Figures 5b and 5e).

In addition to the dependence of the instability growth rate results on the assumed electron distribution function, there is a dependence on the ratio of the densities of hot to cold electrons [Wu et al., 1981b; 1982; Wong et al., 1982; Pritchett, 1984]. When the density of cold electrons is much less than that of the hot electrons, as might be expected in the high altitude portion of the AKR source region, these studies show that wave growth in the X mode can occur for real frequencies less than f_H, which in turn means less than the cold plasma X mode cutoff at f_x. Thus, this effect must be considered when inferences are made concerning propagation modes based on wave cutoff observations. In particular, the detailed investigation of Wong et al. [1982] indicates that X mode AKR can be generated at frequencies below f_x if f_N/f_H is sufficiently small. They find that wave growth occurs at frequencies below f_H for $f_N/f_H = 0.1$ but not for $f_N/f_H = 0.17$ when the ratio of energetic to background electron densities is 10. The maximum altitude of ISIS 1 (3500 km) only extends into the lower portion of the AKR source region, however, and it is unlikely that such energetic to background electron density ratios are appropriate for the ISIS 1 data. This situation is particularly the case for the higher density conditions where the AKR is interpreted as O mode. The example of Figure 13 is a case in point. Here $f_N/f_H = 0.37$ and $f_N = 0.17$ MHz which corresponds to a total (energetic plus background) electron density of $N_e = 3.6 \times 10^2$ cm^{-3}. Thus, the conditions of low f_N/f_H and low N_e for AKR X mode wave growth in the frequency region below f_H are not satisfied in the

case of Figure 13 and the observed AKR is likely in the O mode for the reasons stated at the end of Section 3.

The dramatic high frequency cutoff at $f_H/2$ observed with the whistler mode signals (Figure 5e) strongly suggests that they are received at the satellite via wave mode ducting in field aligned N_e enhancements [see, e.g., Helliwell, 1965]. These observations, together with the indications that the W mode signals are stronger at lower altitudes (see discussion at the beginning of Section 3), support the theoretical work of Wu et al. [1983]. They considered the growth of W mode signals resulting from a loss cone distribution in reflected auroral electrons. Wave growth was found to be limited to low altitudes (below the ISIS 1 apogee of 3500 km) with peak growth rates of emissions beamed downward along the magnetic field direction occurring at real frequencies near 0.6 f_H. The ISIS 1 results suggest that only the reflected waves which are ducted in field aligned density enhancements (and thus restricted to $f < f_{H/2}$) reach the satellite.

AKR frequency gaps

The ionogram signature of an AKR source region encounter is the closing of the frequency gap between the sounder stimulated f_H resonance and the AKR fundamental signal together with the presence of harmonic AKR signals greater than the 2nd [Benson and Calvert, 1979; Calvert, 1981a]. A number of theoretical investigations of the cyclotron maser mechanism have concluded that the frequency gap between f_H and the fundamental X mode AKR peak growth rate is in the range from 1 to 6% of f_H [Wu and Lee, 1979; Lee et al., 1980; Omidi et al., 1982; Wu et al., 1982; Wong et al., 1982; Hewitt and Melrose, 1983; Omidi et al., 1984; LeQueau et al., 1984a]. Since f_H is typically 450 kHz in the present ISIS 1 data set (see Figure 23), the theoretical frequency gaps are within 1/2 the receiver bandwidth of 50 kHz. Thus, from the observa-

tional point of view, these theoretical frequency gaps would all fall into the "zero gap" condition on ISIS 1 ionograms. Even the theoretically predicted banded structure due to the 2 frequency growth bands of the fundamental X mode AKR fall within this zero gap region and thus it could not correspond to the banded structure observed on the fundamental AKR on ISIS 1 ionograms as suggested by Hewitt and Melrose [1983]. The observed frequency gap to the 2nd band is of the order of tens of percent of f_H (see, e.g., Figure 5 of Benson [1982a] for a particularly clear example) and most likely represents AKR from a remote source as discussed near the end of Section 5 in connection with Figure 26. Theoretical investigations of the AKR 2nd harmonic X mode indicate that the corresponding frequency gap to $2f_H$ is also at most a few percent [Lee et al., 1980; Wu and Qiu, 1983]. The dependence of the observed fundamental and 2nd harmonic frequency gaps on AKR signal intensity and the number of harmonics observed is indicated in Figure 31. Here it is seen that as the AKR signal intensity increases, and/or the number of harmonic AKR bands increases, the frequency gaps decrease. These results support the findings of Benson and Calvert [1979] and Calvert [1981a] concerning the frequency gap at the fundamental.

The simultaneous occurrence of intense AKR with multiple harmonics and no frequency gap on the fundamental was considered as a signature of an AKR source encounter by Benson and Calvert [1979] and Calvert [1981a]. As pointed out at the end of the last section,however, a comparison of satellite positions corresponding to zero gap conditions with those of multiple harmonic conditions yields slight differences. These differences may be significant in that the limited latitudinal range over which harmonics higher than the 2nd are observed, as compared to fundamental and 2nd harmonic AKR, suggests that the higher harmonics are much weaker and/or that they are rapidly damped as

they propagate away from their source region. This source region is centered on 70^{o} Λ (Figures 17d and 17g) which corresponds to the latitude of most frequent occurrence of late evening inverted V electron precipitation [Hoffman and Lin, 1981].

AKR harmonics

As pointed out above, propagation effects appear to be much more important for the X mode 2nd harmonic than for the higher harmonics (see also the discussion at the end of Section 4). Such propagational effects could explain the 2nd to fundamental frequency ratio results of Figure 21. As pointed out by Benson and Calvert [1979], the maximum frequency recorded by ISIS 1 for the fundamental AKR band corresponds to signals from the lowest altitude portion of the AKR source region. Thus propagation effects play an important role in interpreting the observed maximum frequency.

Two major factors must be considered when comparing the effects of wave propagation on fundamental and 2nd harmonic X mode AKR, namely, the initial propagation angle and wave refraction. The growth rate calculations of Lee et al. [1980] and Hewitt et al. [1982] indicate that maximum wave growth occurs for both cases when the wave propagation vectors are directed upward but at a large angle to the magnetic field direction, with the 2nd harmonic making a larger angle (i.e., more nearly perpendicular propagation) than the fundamental. Once the waves are generated, upward wave refraction will have a greater effect on the fundamental than the 2nd harmonic because the fundamental is generated near the wave cutoff frequency f_x. Thus, both factors work toward directing X mode AKR at the fundamental more in the upward direction than the 2nd harmonic. When the satellite is close to the source region, the altitude below the satellite responsible for generating fundamental X mode AKR corresponding to the maximum observed frequency XM1(max) will generate 2nd

harmonic waves which will pass under the satellite. Second harmonic waves capable of reaching the satellite will originate at greater altitudes. Since the AKR frequency decreases with increasing altitude, XM2(max) will be less than 2[XM1(max)] as observed in Figures 21a, 21b and 21c.

In addition to propagation effects, wave cutoff limitations enter into the interpretation of the ratios of 2nd harmonic to fundamental X mode minimum frequencies of Figure 21d, 21e and 21f. Since many of the minimum frequencies correspond to locally generated signals during source encounters, especially many of the intensity 3 cases of Figure 21d, propagation effects are not a major factor. These "zero frequency gap" cases (on both the 2nd harmonic and the fundamental) are responsible for the distribution of frequency ratios involving intensity 3 fundamental signals centered around 2 in Figure 21d. As the signal intensity decreases (Figures 21e and 21f), presumably corresponding in most cases to more distant sources, propagation effects become more important and the fundamental signal reception is limited to frequencies above wave cutoff at f_x. The result is a distribution of XM2(min) < 2[XM1(min)] as clearly evident in Figure 21f as well as in Figure 8h.

Wu and Qiu [1983] recently considered 2nd harmonic AKR in more detail. They treat the 2nd harmonic always as X mode. Observationally, however, there appears to be two distinct types of 2nd harmonic AKR which in this work have been classified as O and X modes, the former occurring predominately below $2f_H$ when f_N/f_H is small (see Figures 8f and 8i) and the latter above $2f_H$ (Figures 8b, 8e and 8h). An ionogram illustrating both types of 2nd harmonic AKR, with corresponding fundamental AKR bands, is presented in Figure 32. Here it is clearly seen that there are two distinct 2nd harmonic signals (most apparent in the first 10 msec of delay time) with the one labeled as O mode extending well below $2f_H$ and the one labeled as X mode limited to the frequency region

above $2f_H$. These signals could also be interpreted as the two X mode 2nd harmonic components predicted by Wu and Qiu [1983]. In this interpretation the signal labeled OM2 would correspond to a downward propagating 2nd harmonic X mode component which is generated in the frequency range below $2f_H$ while the signal labeled XM2 would correspond to an upward propagating 2nd harmonic X mode component generated in the frequency range above $2f_H$. As mentioned earlier, however, the 2nd harmonic O mode label was given to signals with an observed harmonic relationship to fundamental AKR signals that extend well into the frequency domain below f_x (such as OM1 in Figure 32) - and thus are not in the X mode. The distribution of the ratios of minimum frequency to f_H for all of the 2nd harmonic AKR are presented in Figure 33. If all 2nd harmonic AKR bands are to be interpreted as X mode (as in the work of Wu and Qiu [1983]), then the histograms of Figures 33a and 33b should be combined. The result of such a combined data base would indicate that 2nd harmonic AKR in the frequency range below $2f_H$ occurs very infrequently compared with 2nd harmonic AKR above $2f_H$.

The N_e cavity

The N_e cavity associated with the AKR source region can be much broader in latitude than the corresponding dimensions of inverted V electron precipitation structures, AKR source regions or discrete auroral arcs (see Figures 27 and 28 and Figures 3-7 of Benson and Akasofu [1984]). The latitudinal width of the cavity at ISIS 1 altitudes is consistent with the broad lower extent of the AKR N_e cavity deduced from Hawkeye data by Calvert [1981b]. Evidence that inverted V, discrete auroral arc and AKR source structures within this cavity are relatively stable in space over time intervals of minutes is provided by correlative studies between AKR and energetic electron data (Figure 26) and ground based auroral observations (see, e.g., Figure 3 of Benson and Akasofu

[1984]). Additional evidence for such stability is provided by the AE-D low energy electron observatins of inverted V structures which suggests that they are time stationary during the passage of the satellite through the structure [Hoffman and Lin, 1981] since inverted V precipitation and AKR have been observed to be closely correlated [Benson and Calvert, 1979; Green et al., 1979; Benson et al., 1980]. This inverted V stability question was addressed further in the recent DE-1/DE-2 correlative study of Thieman and Hoffman [1984]. They present evidence that inverted V precipitation can remain stable over time spans as great as 18 minutes. Not all events are so stable, however, and it was concluded that a series of inverted V events come and go over a range of invariant latitudes on a given night. If the parallel electric fields associated with inverted V precipitation (see, e.g., Kan and Lee [1981]) deplete the background electron density as proposed by Wu and Lee [1979], and if the time scale for density recovery is long compared to the depletion time scale, then a large N_e cavity should develop as auroral activity builds up during the course of the evening. In general, this depleted region will be larger than the region of AKR generation encountered during the time interval of several minutes required for the passage of ISIS 1 through the high altitude auroral region (compare the latitudinal coverage of the AKR source field line projections with the latitudinal extent of the log $N_e(cm^{-3}) = 2$ curves in Figures 27 and 28 and Figures 3-7 of Benson and Akasofu [1984]). Within this main N_e depletion region there could be further isolated depletions below the ISIS 1 detection threshold of $N_e \approx 30$ cm^{-3} which are associated with individual AKR source encounters.

There are no such limitations on measuring electron density enhancements. Indeed the combination of data from the topside sounder and the cylindrical electrostatic probe experiments on ISIS 1 are ideal for investigating N_e

enhancements within the AKR N_e cavity. The lack of large enhancements in this region (as indicated by the results of Figure 27) does not support the mode conversion mechanism of Jones et al. [1984] which would require rod-like N_e enhancements of more than 2 orders of magnitude to obtain the required $f_N = 2f_H$ at a radio window where the waves can escape. Similarly, the great variability of the shape and latitudinal extent of the N_e cavities relative to the location of AKR source field lines in Figures 27 and 28 and Figures 3-7 of Benson and Akasofu [1984] does not support the mode conversion mechanism of Oya and Morioka [1983]. They require that the AKR wave frequency equals f_N at the point where the Z to O mode conversion takes place. For a frequency of 500 kHz this requirement implies that the mode conversion takes place at the $N_e = 3 \times 10^3$ cm^{-3} contours of Figures 27 and 28 and Figures 3-7 of Benson and Akasofu [1984]. A wide variety of propagation conditions would be required for waves originating at these contours to explain all of the observed AKR in terms of O mode AKR from the conversion mechanism. Electron density enhancements are not required, on the other hand, in the basic cyclotron maser mechanism of Wu and Lee [1979] and the enhancements required by the feedback model of Calvert [1982] are well within the range of observed enhancements.

The ISIS 1 data provide relative intensity information between the different modes near and within the AKR N_e cavity. The observations of O mode AKR with greater intensity than X mode AKR near the low latitude cavity boundary (Figure 15) are consistent with the predominance of O mode AKR observed by Jikiken (EXOS-B) equatorward of the cavity [Oya and Morioka, 1983] and the detection of weak O mode AKR near the plasmapause by DE-1 [Huff and Shawhan, 1982]. The near confinement of intensity 3 X mode AKR to the N_e cavity (Figure 15, top) may correspond to the saturation condition in the feedback model of Calvert [1983]. The common occurrence of lower intensity X

mode AKR within the cavity, however, indicates that either saturation does not always occur or the feedback conditions are not always satisfied (Figure 15, middle and bottom; also compare XM1 intensity 1 in Figure 17g with XM1 intensity 3 in Figure 17a). Similarly, the intensity 1 X mode AKR observed outside of the AKR N_e cavity (see the x's in the bottom of Figure 15 and the XM1 histogram in Figure 17g between 50 and 60° Λ) could be due to the lower expected growth rates for the relatively large f_N/f_H values (see Figure 30), the lack of the proper conditions for the feedback mechanism to operate, wave refraction of most of the energy from more intense signals originating from within the cavity or to a combination of these effects.

8. Summary

AKR is commonly observed on high-altitude (near 3500 km apogee) nighttime auroral zone passes of the ISIS 1 satellite. The received signal intensities and wave modes (as deduced from cutoff phenomena) are dependent on the ambient plasma parameter f_N/f_H. Intense AKR is commonly observed in the X mode when $f_N/f_H \lesssim 0.1$, but rarely in the O mode and never in the Z or W mode. Moderate strength AKR is observed in the X mode out to $f_N/f_H \approx 1.0$; it is occasionally observed in the Z mode but never in the W mode. Weak AKR is observed in the X and O modes out to $f_N/f_H \approx 1.1$, in the Z mode over nearly all f_N/f_H sampled and in the W mode when $f_N/f_H \gtrsim 0.6$ (instrumental limitations prevented the detection of W mode signals at low f_N/f_H). There is some evidence that the W mode is stronger at lower altitudes.

The frequency limits are different for the various AKR wave modes. The high frequency limits for the X and O modes appear to correspond to the quenching f_N/f_H value at the bottom of the AKR source region. Often the O mode high frequency limit cannot be determined because of the masking effect of a more intense (at low f_N/f_H) X mode. The low frequency limit of the X

mode is the f_x wave cutoff. The low frequency limit of the O mode is the wave cutoff at f_N when $f_N/f_H \approx 1$. When $f_N/f_H < 1$ the O mode extends only slightly below f_H, suggesting that the waves in this frequency range originate from a source slightly above the satellite. The Z mode occasionally extends from wave cutoff at f_z to wave resonance at f_T; more often, however, it is limited to the frequency range between f_N and f_H. It can be observed with a steady amplitude over time intervals of several seconds. The W mode has a dramatic high frequency cutoff at $f_H/2$, suggesting that the responsible waves are ducted along magnetic field-aligned N_e enhancements to the satellite from a source below. These observations are consistent with recent W mode predictions based on the Doppler shifted cyclotron mechanism [Wu et al., 1983].

Harmonic signals are observed to be associated with X and O mode AKR. The 2nd harmonic X mode AKR observations are consistent with a propagating signal whereas the 3rd and 4th harmonics are likely heavily damped signals that do not propagate far from their low density source region. The 2nd harmonic interpreted as O mode is more often observed at frequencies below $2f_H$ when f_N/f_H is small and above $2f_H$ when it is large. In addition to harmonic signals, the fundamental sometimes reveals a component structure. The frequency separation between these components is far greater than predicted frequency differences between the 2 fundamental growth bands in the Doppler shifted cyclotron mechanism and it is likely due to 2 sources separated in space.

The sounder-derived N_e contours through the AKR source region, together with in situ probe data, indicate that (1) the AKR N_e cavity (i.e., $N_e < 10^2 cm^{-3}$) is often much wider than inverted V precipitation, discrete auroral arcs or AKR sources as detected during a given ISIS 1 pass, (2) the projected $(f_N/f_H)_{max}$ values for X and O mode source encounters agree with theoretical

f_N/f_H values corresponding to the sharp decreases in X and O mode temporal growth rates near f_N/f_H = 0.3 and 1.0, respectively, (3) the most intense AKR cannot be interpreted in terms of O mode signals from radiation at f_N from local N_e enhancements and (4) N_e enhancements sufficient to support a feedback mechanism in the low density AKR source region cannot be ruled out.

Some of the main questions posed by the ISIS 1 data are the following: (1) Why are the X mode harmonic AKR signals of greatest intensity observed predominately under the lowest f_N/f_H ($\lesssim$ 0.1) conditions? (2) Are the higher order X mode harmonics (n = 3 and 4), which appear to be spatially confined, and the X mode 2nd harmonic (which appears capable of propagating great distances) generated by different mechanisms? (3) Are the harmonics observed to be associated with the O mode indeed O mode waves or are they harmonics of X mode waves as suggested by Wu and Qui [1983], or the result of coalescing Z mode waves as suggested by Melrose et al. [1984]. (4) What is the cause of the discrepancy between the theoretical predictions of Melrose et al. [1984], concerning the relative power levels of the X, O and Z mode waves, and the ISIS 1 observations?

Acknowledgements. I am grateful to M. Posey and W. Schar for assistance in the data analysis. I also wish to thank L. Brace for providing the ISIS 1 cylindrical electrostatic probe data and for helpful discussions, H. G. James and D. B. Muldrew for information on the receiver automatic gain control and other aspects of the ISIS 1 system, and W. Calvert and D. M. Klumpar for their part in the preparation of Figure 26 which was almost used in our earlier collaborative effort. I have benefitted greatly by a number of conversations pertaining to AKR with S. A. Curtis, R. G. Hewitt, H. K. Wong and C. S. Wu. Photographic reproductions of the ISIS 1 ionograms were made by the National Space Science Data Center at the Goddard Space Flight Center.

References

Benson, R. F., Source mechanism for terrestrial kilometric radiation, Geophys. Res. Lett., 2, 52-55, 1975.

Benson, R. F., Auroral kilometric radiation source region observations from ISIS 1, in Phys. of Auroral Arc Formation, Geophys. Monogr. Ser., 25, 369-379, AGU, Washington, D.C., 1981.

Benson, R. F., Harmonic auroral kilometric radiation of natural origin, Geophys. Res. Lett., 9, 1120-1123, 1982a.

Benson, R. F., Stimulated plasma instability and nonlinear phenomena in the ionosphere, Radio Sci., 17, 1637-1659, 1982b.

Benson, R. F., Ordinary mode auroral kilometric radiation, with harmonics, observed by ISIS 1, Radio Sci., 19, 543-550, 1984.

Benson, R. F., and W. Calvert, ISIS 1 observations at the source of auroral kilometric radiation, Geophys. Res. Lett., 6, 479-482, 1979.

Benson, R. F., and S.-I. Akasofu, Auroral kilometric radiation/aurora correlation, Radio Sci., 19, 527-541, 1984.

Benson, R. F., W. Calvert, and D. M. Klumpar, Simultaneous wave and particle observations in the auroral kilometric radiation source region, Geophys. Res. Lett., 7, 959-962, 1980.

Bujarbarua, S. and M. Nambu, Auroral kilometric radiation induced by double layers, J. Phys. Soc. Japan, 52, 2285-2288, 1983.

Bujarbarua, S., S. N. Sarma, and M. Nambu, Auroral kilometric radiation due to a new plasma instability, Phys. Rev. A, 29, 2171-2178, 1984.

Calvert, W., The signature of auroral kilometric radiation on ISIS 1 ionograms, J. Geophys. Res., 86, 76-82, 1981a.

Calvert, W., The auroral plasma cavity, Geophys. Res. Lett., 8, 919-921, 1981b.

Calvert, W., A feedback model for the source of auroral kilometric radiation, J. Geophys. Res., 87, 8199-8214, 1982.

Calvert, W., Harmonics and related ISIS-1 AKR observations, EOS, 64, 815, 1983.

Dusenbery, P. B., and L. R. Lyons, General concepts on the generation of auroral kilometric radiation, J. Geophys. Res., 87, 7467-7481, 1982.

Dusenbery, P. B., and L. R. Lyons, Generation of Z mode radiation by diffuse auroral electron precipitation, EOS, 64, 814, 1983.

Freund, H.P., H. K. Wong, C. S. Wu, and M. J. Xu, An electron cyclotron maser instability for astrophysical plasmas, Phys. Fluids, 26, 2263-2270, 1983.

Grabbe, C. L., Auroral kilometric radiation: A theoretical review, Rev. Geophys. Space Res., 9, 627-633, 1981.

Grabbe, C. L., Reply, J. Geophys. Res., 88, 7259-7260, 1983.

Grabbe, C. L., K. Papadopoulos, and P. J. Palmadesso, A coherent nonlinear theory of auroral kilometric radiation 1. Steady state model, J. Geophys. Res., 85, 3337-3346, 1980.

Green, J. L., D. A. Gurnett, and S. D. Shawhan, The angular distribution of auroral kilometric radiation, J. Geophys. Res., 82, 1825-1838, 1977.

Green, J. L., D. A. Gurnett, and R. A. Hoffman, A correlation between auroral kilometric radiation and inverted V electron precipitation, J. Geophys. Res., 84, 5216-5222, 1979.

Green, J. L., N. A. Saflekos, D. A. Gurnett and T. A. Potemra, A correlation between auroral kilometric radiation and field-aligned currents, J. Geophys. Res., 87, 10463-10467, 1982.

Gurnett, D. A., The earth as a radio source: Terrestrial kilometric radiation, J. Geophys. Res., 79, 4227-4238, 1974.

Gurnett, D. A., High latitude electromagnetic plasma wave emissions, in High-Latitude Space Plasma Physics, edited by Bengt Hultqvist and Tor Hagfors, pp. 355-375, Plenum Publishing Corporation, 1983.

Gurnett, D. A., and J. L. Green, On the polarization and origin of auroral kilometric radiation, J. Geophys. Res., 83, 689-696, 1978.

Gurnett, D. A., R. R. Anderson, F. L. Scarf, R. W. Fredricks and E. J. Smith, Initial results from the ISEE 1 and 2 plasma wave investigation, Space Sci. Rev., 23, 103-122, 1979.

Gurnett, D. A., S. D. Shawhan, and R. R. Shaw, Auroral Hiss, Z mode radiation, and auroral kilometric radiation in the polar magnetosphere: DE 1 observations, J. Geophys. Res., 88, 329-340, 1983.

Hagg, E. L., E. J. Hewens, and G. L. Nelms, The interpretation of topside sounder ionograms, Proc. IEEE, 57, 949-960, 1969.

Helliwell, R. A., Whistlers and Related Ionospheric Phenomena, 349 pp., Stanford University Press, Stanford, 1965.

Hewitt, R. G., and D. B. Melrose, Electron cyclotron maser emission near the cutoff frequencies, Aust. J. Phys., 36, 725-743, 1983.

Hewitt, R. G., D. B. Melrose, and K. G. Ronnmark, The loss-cone driven electron-cyloctron maser, Aust. J. Phys., 35, 447-471, 1982.

Hewitt, R. G., D. B. Melrose, and G. A. Dulk, Cyloctron maser emission of auroral Z mode radiation, J. Geophys. Res., 88, 10065-10071, 1983.

Hoffman, R. A., and C. S. Lin, Study of inverted-V auroral precipitation events, in Phys. of Auroral Arc Formation, Geophys. Monogr. Ser., 25, 80-90, AGU, Washington, D.C., 1981.

Huff, R. L. and S. D. Shawhan, Plasma wave polarization and propagation direction measured with DE-1, EOS, 63, 1075-1076, 1982.

Istomin, Y. N., and O. A. Pokhotelov, Linear conversion of a slow extraordinary wave into a fast wave near the upper hybrid resonance application to terrestrial kilometer-wavelength emission, Sov. J. Plasma Phys., 9, 146-148 (Engl. Transl. of Fiz. Plazmy, 9, 250-253), 1983.

Jackson, J. E., The reduction of topside ionograms to electron-density profiles, Proc. IEEE, 57, 960-976, 1969.

James, H. G., A radio noise band observed near the cleft region, The Second Magnetospheric Cleft Symposium: AGU Chapman Conference, St. Jovite, Quebec, October 1976.

James, H. G., Direction-of-arrival measurements of auroral kilometric radiation and associated ELF data from ISIS 1, J. Geophys. Res., 85, 3367-3375, 1980.

Jones, D., Mode-coupling of Z-mode waves as a source of terrestrial kilometric and Jovian decametric radiations, Astron. Astrophys., 55, 245-252, 1977.

Jones, D., G. Gapper, and R. Herring, Auroral kilometric radiation from field-aligned plasma density enhancements, Annales Geophysicae, 2, 95-104, 1984.

Kan, J. R., and L. C. Lee, Formation of auroral arcs and inverted V precipitations: an overview, in Phys. of Auroral Arc Formation, Geophys. Monogr. Ser., 25, 206-217, AGU, Washington, D.C., 1981.

Kaiser, M. L., J. K. Alexander, A. C. Riddle, J. B. Pearce, and J. W. Warwick, Direct measurements by Voyagers 1 and 2 of the polarization of terrestrial kilometric radiation, Geophys. Res. Lett., 5, 857-860, 1978.

Lee, L. C., J. R. Kan, and C. S. Wu, Generation of auroral kilometric radiation and the structure of auroral acceleration region, Planet. Space Sci., 28, 703-711, 1980.

LeQueau, D., R. Pellat, and A. Roux, Direct generation of the auroral kilometric radiation by the maser synchrotron instability: an analytical approach, Phys. Fluids, 27, 247-265, 1984a.

LeQueau, D., R. Pettat, and A. Roux, Direct generation of the auroral kilometric radiation by the maser synchrotron instability. Physical mechanism and parametric study, J. Geophys. Res., 89, 2831-2841, 1984b.

Lin, C. S., and R. A. Hoffman, Observations of inverted-V electron precipitation, Space Sci. Rev., 33, 415-457, 1982.

Lyons, L. R., and P. B. Dusenbery, A simple expression for kilometric radiation growth rates and analytical applications, J. Geophys. Res., 89, 1009-1014, 1984.

Maggs, J. E., and A. Roux, Comment on "A coherent nonlinear theory of auroral kilometric radiation 1. Steady state model", by C. L. Grabbe et al., J. Geophys. Res., 88, 7256-7258, 1983.

Melrose, D. B., An interpretation of Jupiter's decametric radiation and the terrestrial kilometric radiation as direct amplified gyroemission, Astrophys. J., 207, 651-662, 1976.

Melrose, D. B., K. G. Ronnmark, and R. G. Hewitt, Terrestrial kilometric radiation: The cyloctron theory, J. Geophys. Res., 87, 5140-5150, 1982.

Melrose, D. B., R. G. Hewitt, and G. A. Dulk, Electron-cyclotron maser emission: relative growth and damping rates for different modes and harmonics, J. Geophys. Res., in press, 1984.

Mizera, P. F. and J. P. Fennell, Signatures of electric fields from high and low altitude particle distributions, Geophys. Res. Lett., 4, 311-314, 1977.

Muldrew, D. B., Preliminary results of ISIS 1 concerning electron-density variations, ionospheric resonances and Cerenkov radiation, in Space

Research X, Edited by T. M. Donahue, P. A. Smith, and L. Thomas, pp. 786-794, North Holland Publishing Company, Amsterdam, 1970.

Omidi, N., and D. A. Gurnett, Growth rate calculations of auroral kilometric radiation using the relativistic resonance condition, J. Geophys. Res., 87, 2377-2382, 1982.

Omidi, N., C. S. Wu, and D. A. Gurnett, Generation of auroral kilometric and Z-mode radiation by the cyclotron maser mechansim, J. Geophys. Res., 89, 883-895, 1984.

Oya, H., Origin of Jovian decameter wave emissions - Conversion from the electron cyclotron plasma wave to the ordinary mode electromagnetic wave, Planet. Space Sci., 22, 687-708, 1974.

Oya, H., and A. Morioka, Observational evidence of Z and L-O mode waves as the origin of auroral kilometric radiation from the Jikiken (EXOS-B) satellite, J. Geophys. Res., 88, 6189-6203, 1983.

Pritchett, P. L., Relativistic dispersion and the generation of auroral kilometric radiation, Geophys. Res. Lett., 11, 143-146, 1984.

Ratcliffe, J. A., The Magneto-Ionic Theory and its Applications to the Ionosphere, 206 pp., Cambridge University Press, New York, 1959.

Shawhan, S. D., and D. A. Gurnett, Polarization measurements of auroral kilometric radiation by Dynamics Explorer-1, Geophys. Res. Lett., 9, 913-916, 1982.

Stix, T. H., The Theory of Plasma Waves, 283 pp., McGraw-Hill, New York, 1962.

Theiman, J. R., and R. A. Hoffman, Determination of inverted-V stability from Dynamics Explorer satellite data, submitted to J. Geophys. Res., 1984.

Wagner, J. S., L. C. Lee, C. S. Wu, and T. Tajima, Computer simulation of auroral kilometric radiation, Geophys. Res. Lett., 10, 483-486, 1983.

Wagner, J. S., L. C. Lee, C. S. Wu, and T. Tajima, A simulation study of the loss-cone driven cyclotron maser applied to auroral kilometric radiation, Radio Sci., 509-518, 1984.

Wong, H. K., Excitation of z mode radiation by cyclotron maser instability, EOS, 64, 814, 1983.

Wong, H. K., C. S. Wu, F. J. Ke, R. S. Schneider, and L. F. Ziebell, Electromagnetic cyclotron-loss-cone instability associated with weakly relativistic electrons, J. Plasma Phys., 28, 503-525, 1982.

Wu, C. S., The source mechanism of auroral kilometric radiation, in Phys. of Auroral Arc Formation, Geophys. Monogr. Ser., 25, 418-427, 1981.

Wu, C. S. and L. C. Lee, A theory of the terrestrial kilometric radiation, Astrophys. J., 230, 621-626, 1979.

Wu, C. S., and X. M. Qiu, Emissions of second-harmonic auroral kilometric radiation, J. Geophys. Res., 88, 10072-10080, 1983.

Wu, C. S., S. T. Tsai, M. J. Xu and J. W. Shen, Saturation and energy-conversion efficiency of auroral kilometric radiation, Astrophys. J., 248, 384-391, 1981a.

Wu, C. S., C. S. Lin, H. K. Wong, S. T. Tsai, and R. L. Zhou, Absorption and emission of extraordinary-mode electromagnetic waves near cyclotron frequency in nonequilibrium plasmas, Phys. Fluids, 24, 2191-2196, 1981b.

Wu, C. S., H. K. Wong, D. J. Gorney, and L. C. Lee, Generation of the auroral kilometric radiation, J. Geophys. Res., 87, 4476-4488, 1982.

Wu, C. S., D. Dillenburg, L. F. Ziebell, and H. P. Freund, Excitation of whistler waves by reflected auroral electrons, Planet. Space Sci., 31, 499-507, 1983.

Table 1. Dates of the 12 ISIS 1 passes used in the present study. Also presented are the number of ionograms used in each pass to obtain vertical N_e profiles, the universal time and geographic latitude of the first and last ionogram, the availability of ISIS 1 cylindrical electrostatic probe data and references to ionogram illustrations and N_e contour data corresponding to each pass.

Date			Number of	First ionogram		Last ionogram		CEP	Ionograms used in published illustrations	Curved-earth
Yr	Mo	Day	ionograms	UT	gg Lat.	UT	gg Lat.	data	(including present paper)	N_e contours
69	8	3	11	1256:21	-63.9	1301:04	-53.6	YES		Fig. 28d
69	8	7	8	1320:08	-54.2	1323:24	-47.4	YES	#1-5 as a-e in Fig. 1 of Benson et al. [1980]	Fig. 28c
69	8	8	24	0829:36	-67.8	0840:20	-45.3	YES	#10-13 as a-d in Fig. 3 of Benson et al. [1980]; #16 in Fig. 13	Fig. 28f
69	8	17	25	0839:35	-70.7	0850:43	-48.3	NO	#12-17 as a-f in Fig. 2 of Benson et al. [1980]; #20 in Fig. 32	Fig. 28b
69	8	19	21	0959:08	-59.4	1008:24	-40.9	YES	#7 and 13 in Figs. 5 and 3, respectively of Benson [1982a]; #6-12 as a-g in Fig. 26	Fig. 27
69	10	31	20	1349:47	65.7	1358:34	46.3	YES	#7 and 10 in Figs. 10 and 7, respectively of Benson [1982a]; #16 and 19 in Figs. 4a and 4b, respectively of Benson [1984]; #7-12 as a-f in Fig. 25	[Benson and Akasofu, 1984; Fig. 6]
69	11	26	10	0618:17	59.0	0622:29	50.6	YES	#3-8 as a-f in Fig. 2 of Benson and Calvert [1979]	Fig. 28a
69	12	2	21	0954:23	69.1	1003:47	49.9	YES	#7, 8 and 10 as a, b, and c, respectively in Fig. 5 of Benson and Akasofu [1984]	[Benson and Akasofu, 1984; Fig. 5]
70	11	6	12	0707:47	67.1	0718.18	45.3	YES	#8 in Fig. 3 of Benson and Calvert [1979]	Fig. 28e
70	12	5	10	0630:48	77.3	0639.27	59.6	YES	#7-9 as a-c in Fig. 4 of Benson and Akasofu [1984]	[Benson and Akasofu, 1984; Fig. 4]
70	12	8	14	0718:51	71.8	0731:25	44.4	YES	#6 and 7 as a and b in Fig. 7 of Benson and Akasofu [1984]	[Benson and Akasofu, 1984; Fig. 7]
71	10	29	16	0711:01	84.1	0725:27	51.8	NO	#9 in Fig. 4 of Benson [1982a]; #12 in Fig. 2 of Benson [1982a] and Fig. 1 of Benson and Akasofu [1984]; #9-16 as a-h in Fig. 2 of Benson and Akasofu [1984]	[Benson and Akasofu, 1984 Fig. 3]

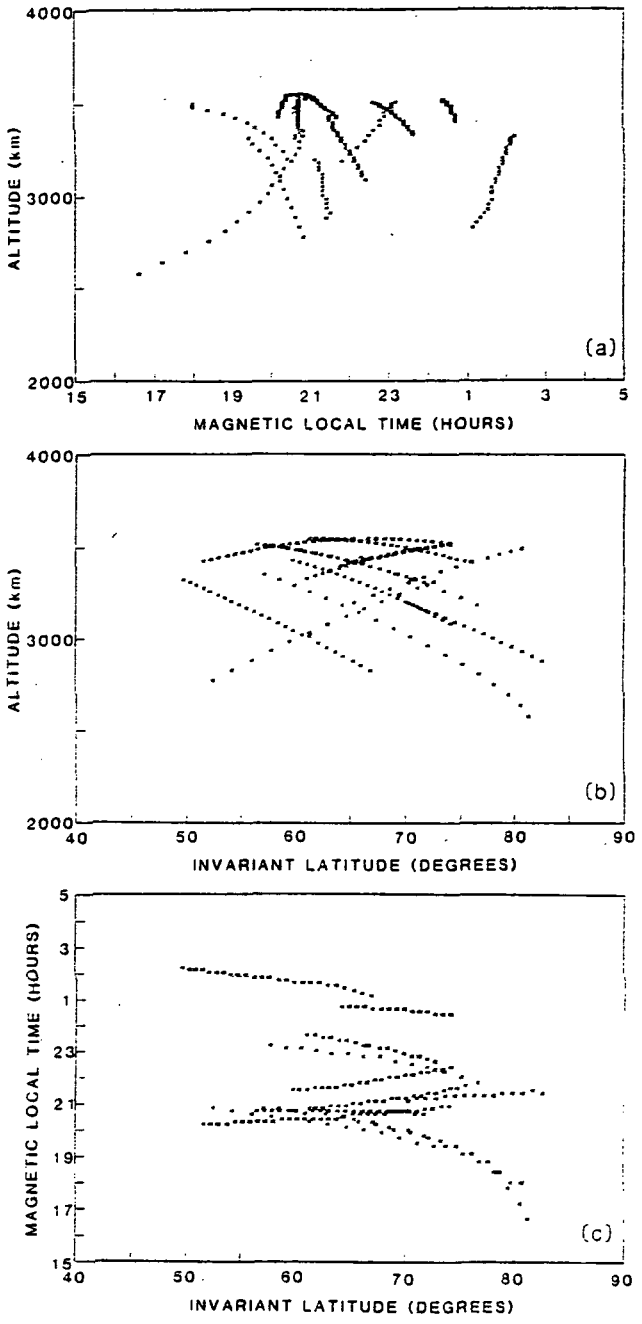

Figure 1. Distribution of 226 ISIS 1 ionograms from 12 passes (see Table 1) used in the present investigation: satellite altitude against magnetic local time MLT (a) and invariant latitude (b), and the corresponding values of MLT and Λ for each satellite position (c). Note: more ionograms were investigated for natural noise than were used to obtain vertical N_e profiles, i.e., the 226 represented here (corresponding to the data of Figures 2-9, 14-24, 29, 31 and 33) vs. the 192 represented in Table 1 (corresponding to the data of Figures 27, 28, and 30).

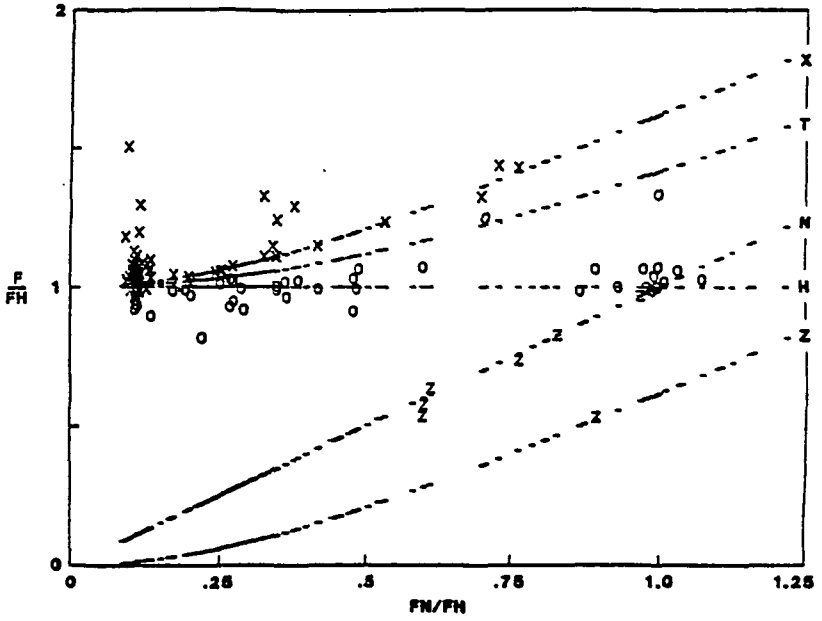

Figure 2. Normalized minimum frequencies of moderate to intense AKR (intensities 2 or 3) identified as X, O or Z mode organized according to the value of f_N/f_H at the point of observation. The horizontal dashes identify scaled or calculated values of f_X, f_T, f_N, f_H and f_Z for each ionogram and are designated on the right hand side by X, T, N, H and Z, respectively.

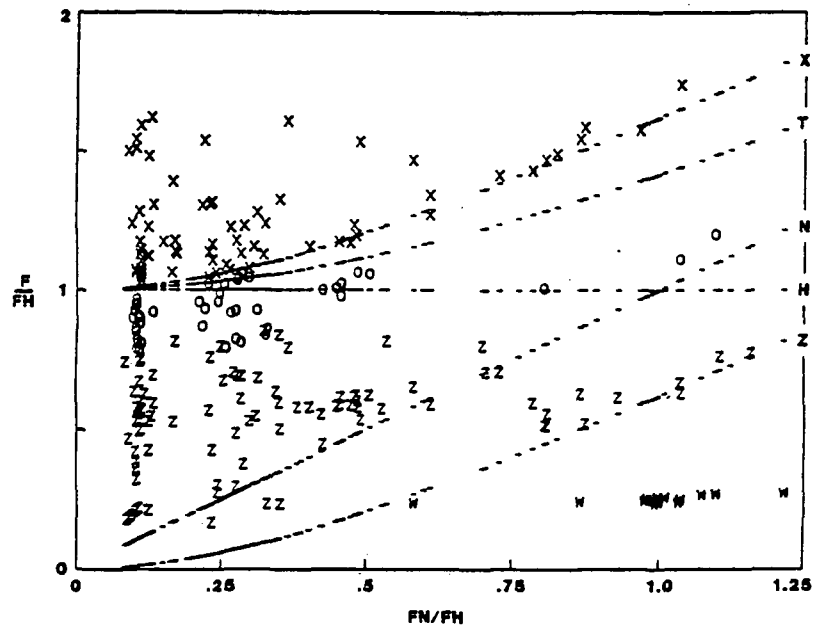

Figure 3. Same as Figure 2 except for weak AKR (intensity 1). In this case signals attributed to the whister (W) mode are also observed.

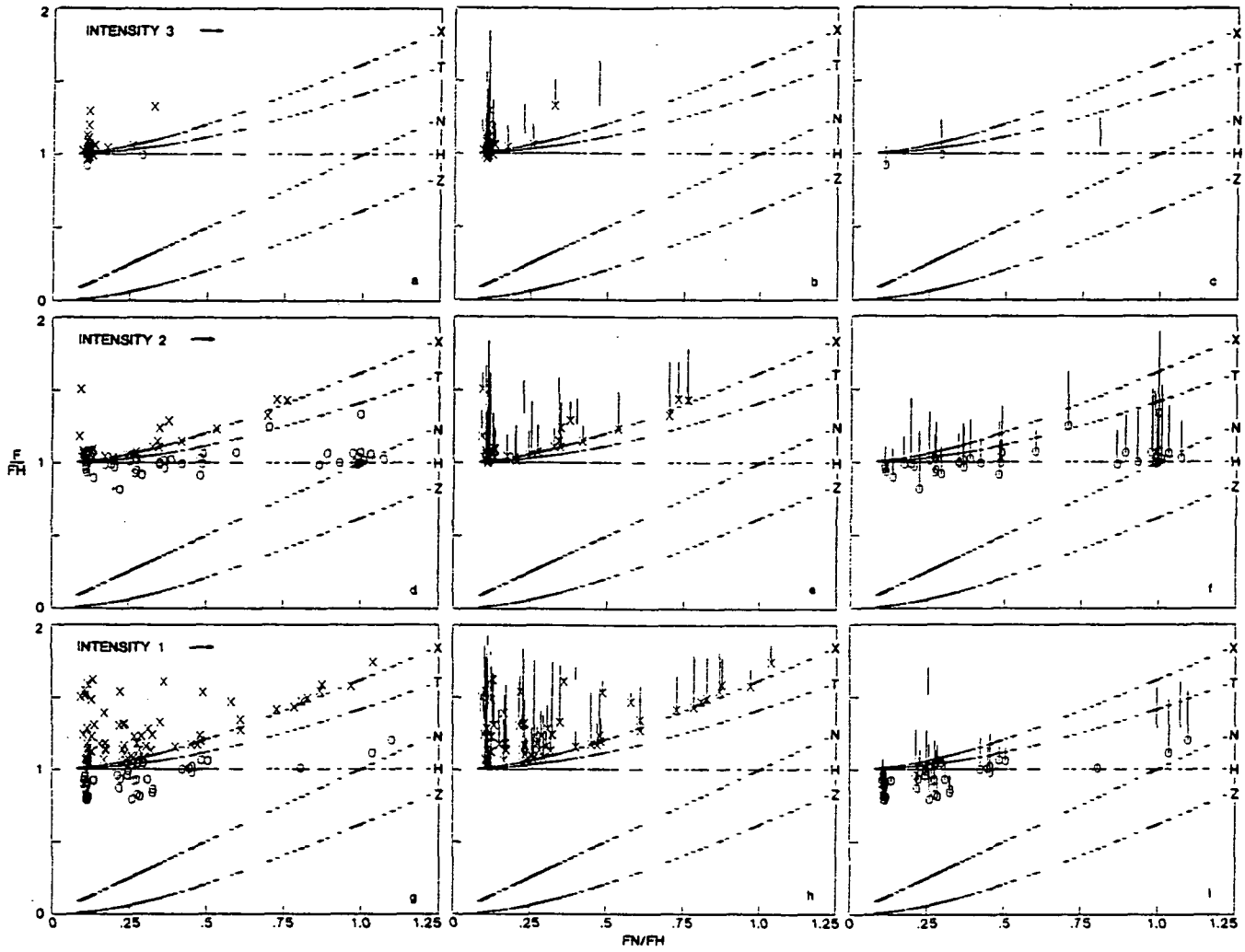

Figure 4. Breakdown of the X and O mode data of Figures 2 and 3 by signal intensity (a, d and g) including the AKR normalized frequency bandwidth separately for the X and O modes in b, e and h and c, f and j, respectively.

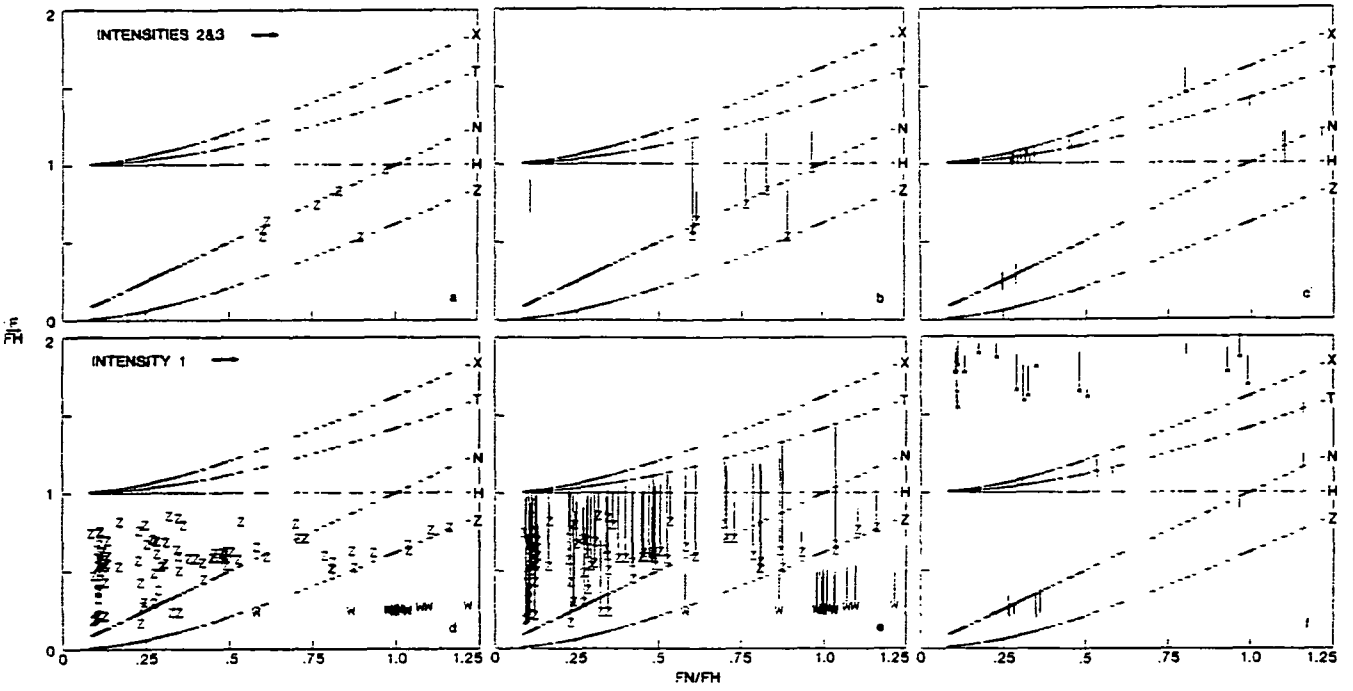

Figure 5. Breakdown of the Z and W mode data of Figures 2 and 3 by signal intensity (a and d) including the normalized frequency bandwidths for Z and W (b and e) and "other" signals (c and f).

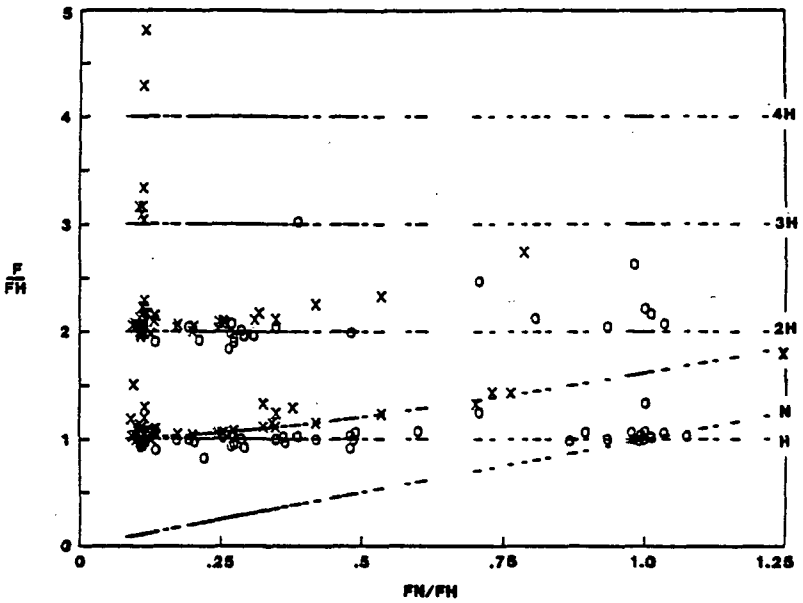

Figure 6. Same as Figure 2, i.e., moderate to intense AKR (intensities 2 or 3), with the addition of the X and O mode harmonic noise bands and the scaled or calculated values of $2f_H$, $3f_H$ and $4f_H$ designated by 2H, 3H and 4H, respectively.

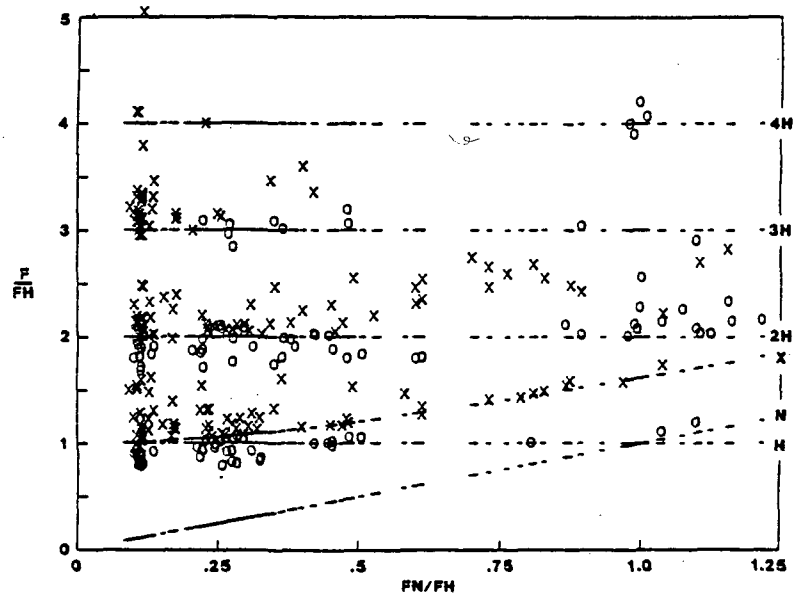

Figure 7. Same as Figure 6 except for weak AKR (intensity 1).

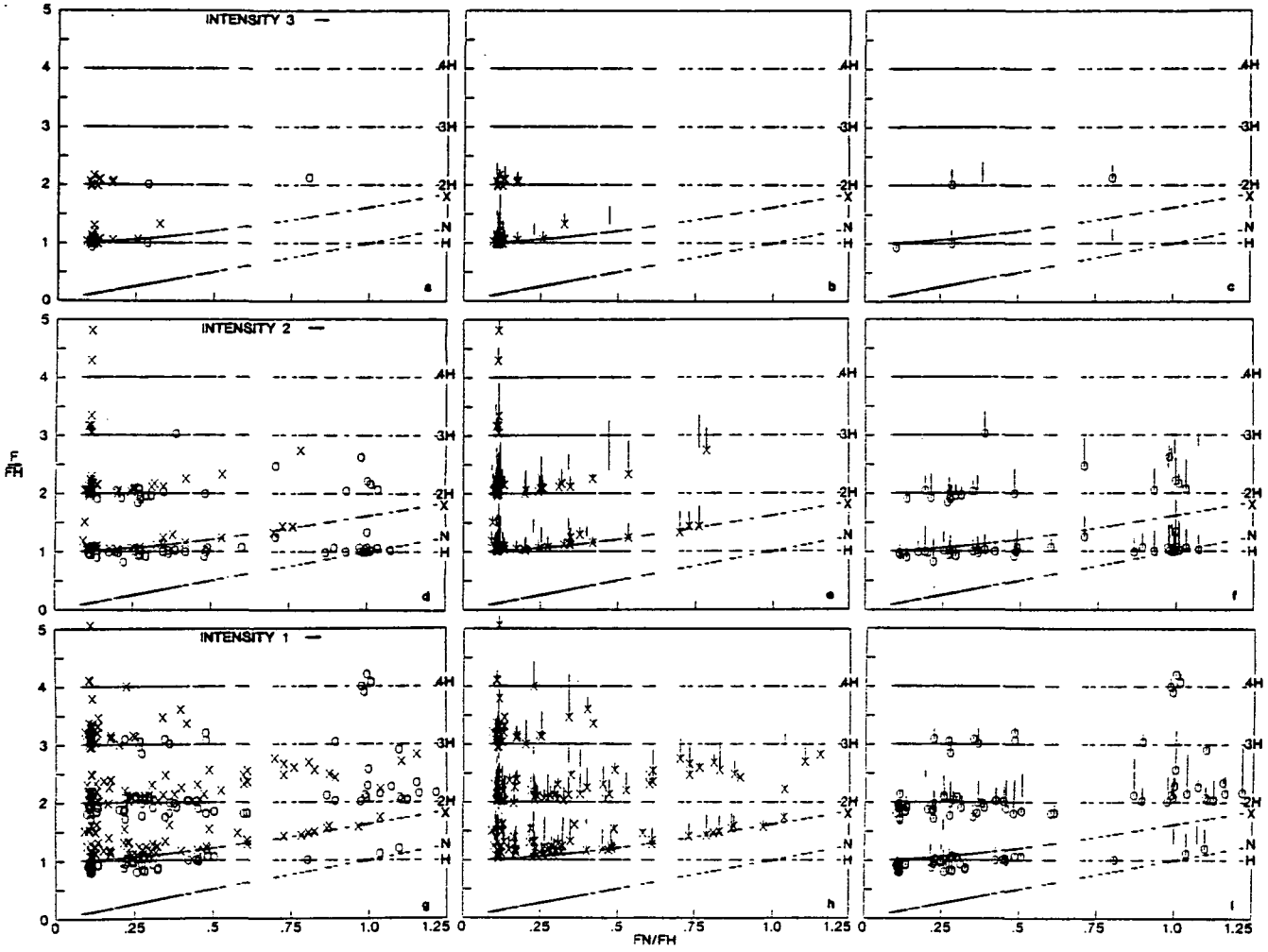

Figure 8. Breakdown of the X and O mode data of Figures 6 and 7 by signal intensity (a, d and g) including the AKR normalized frequency bandwidths separately for the X and O modes in b, e and h and c, f and i, respectively.

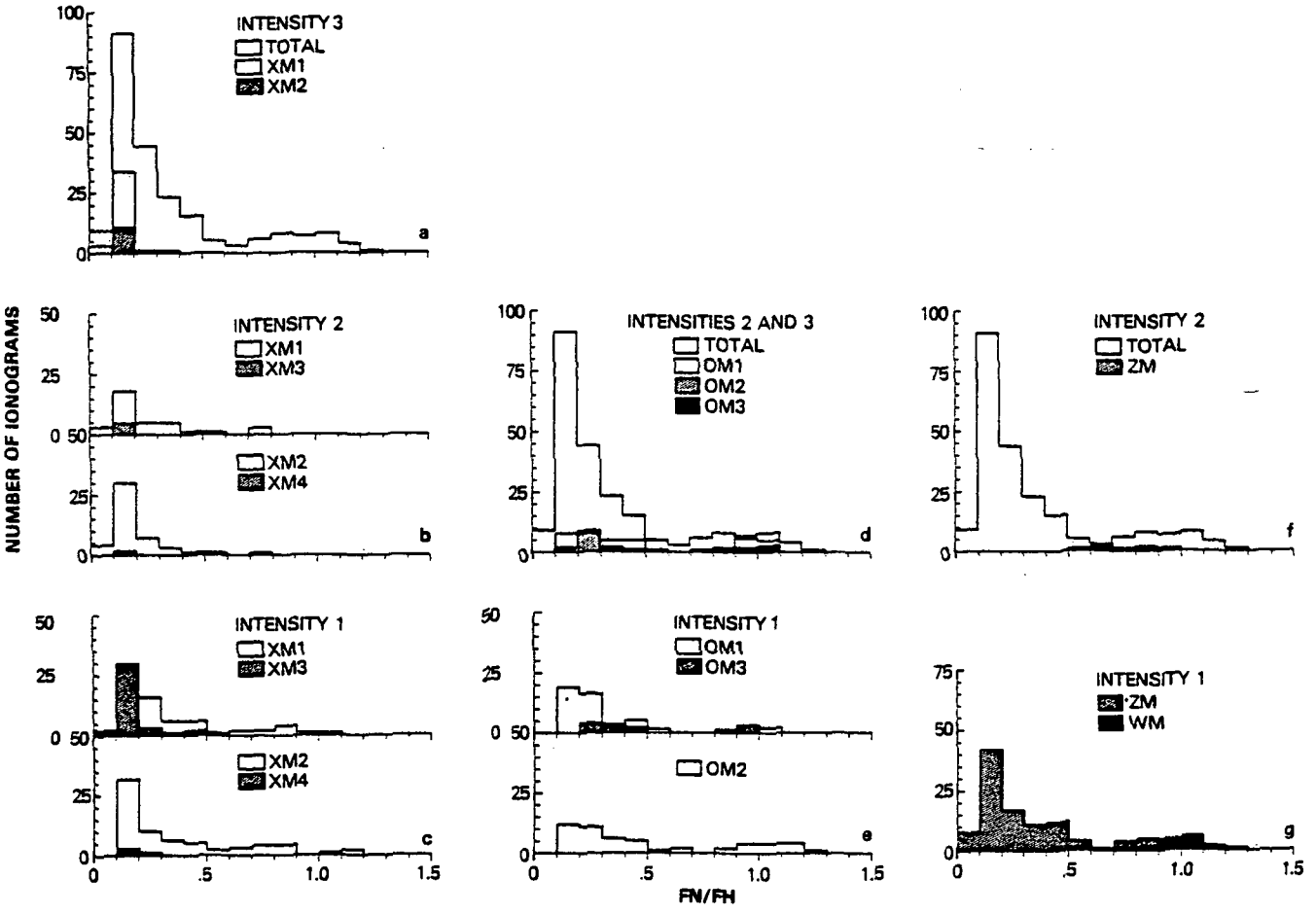

Figure 9. Histogram presentation of the distribution of ionograms containing the data of Figures 5a, 5d, 8a, 8d and 8g. The X mode fundamental, 2nd, 3rd, and 4th harmonic AKR bands are designated as XM1, XM2, XM3 and XM4, respectively (in a, b and c). Similarly, the O mode AKR bands are designated as OM1, OM2 and OM3 in d and e (the single OM3 intensity 2 signal in d is in the 0.3 to 0.4 f_N/f_H interval). The Z and W mode signals are designated as ZM and WM in f and g (no intensity 2 W mode signals were observed in the present data set). Some of the data entries in the f_N/f_H 0 to 0.1 and 0.1 to 0.2 ranges correspond to upper limit values where f_N could merely be determined to be less than 50 kHz, e.g., see Figure 5 of Benson et al. [1980].

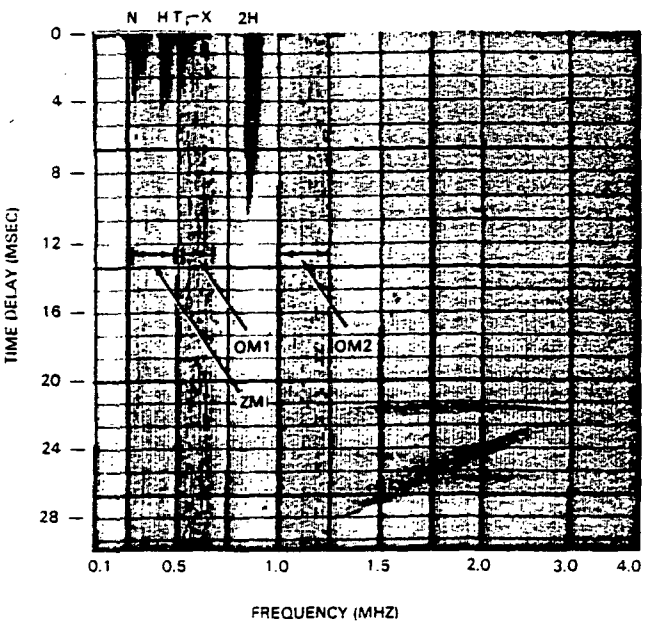

Figure 10. ISIS 1 ionogram illustrating the natural noise signals identified as Z mode and fundamental and 2nd harmonic O mode AKR. Sounder-stimulated plasma resonances at f_N, f_H, f_T and $2f_H$ are labeled at the top of the figure by N, H, T and 2H, respectively. The X mode cutoff frequency f_x is labeled by an X. Long-range sounder-generated ionospheric echoes are observed between 1.25 and 3.0 MHz corresponding to time delays greater than 20 msec. (19 August 1969, 1009 UT, 39°S, 148°E, 3502 km, 2018 MLT, 58° Λ, f_N/f_H = 0.71.)

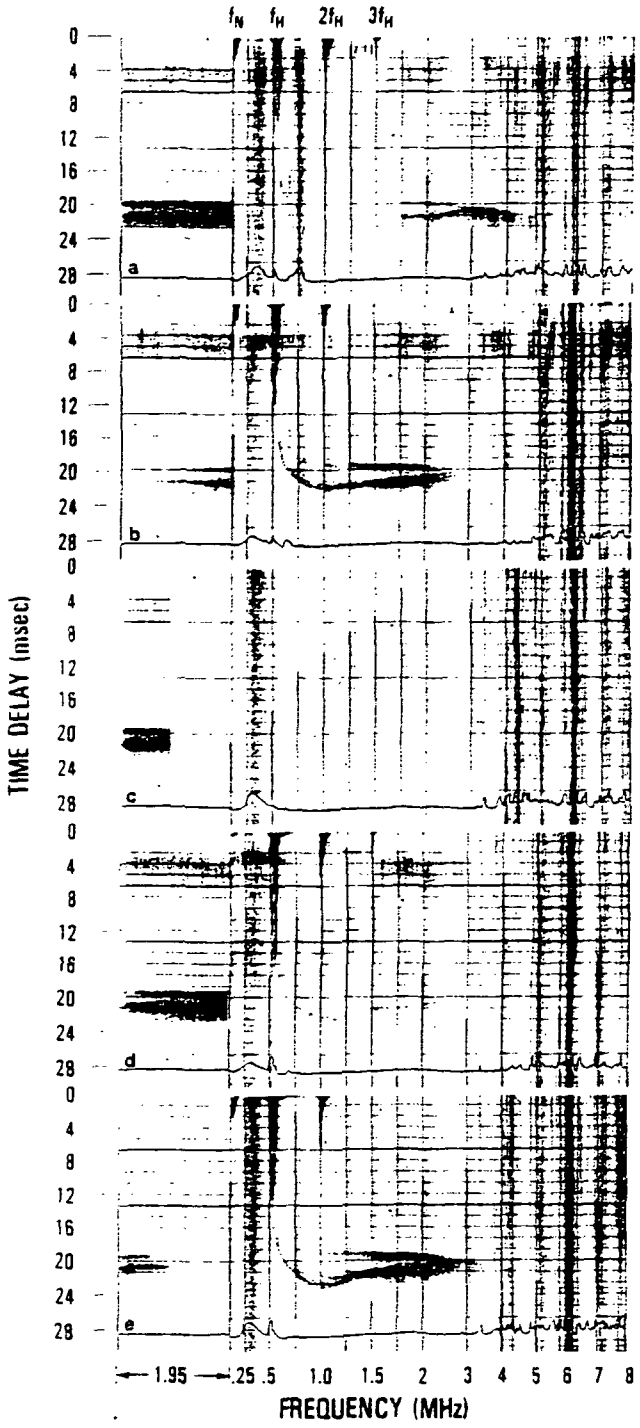

Figure 11. Natural Z mode noise observed between the plasma frequency f_N and the electron gyrofrequency f_H by the ISIS 1 topside sounder. Plasma resonances, which are identified at the top of the figure, are stimulated by the pulses from the swept-frequency sounder on ionograms a, b, d, and e. The sounder instrument was changed to a sounder-off mode during the fixed frequency portion of ionogram c and returned to a sounder-on mode before the recording of ionogram d. The receiver automatic gain control (AGC) voltage at the bottom of each ionogram has been enhanced for visibility. The satellite altitude, invariant latitude and magnetic local time ranged from 3155 km, 76° and 0042 in a to 3103 km, 74° and 0044 in e over Resolute Bay, NWT (27 June 1974, 0534 to 0535 UT, with 18 sec between ionograms).

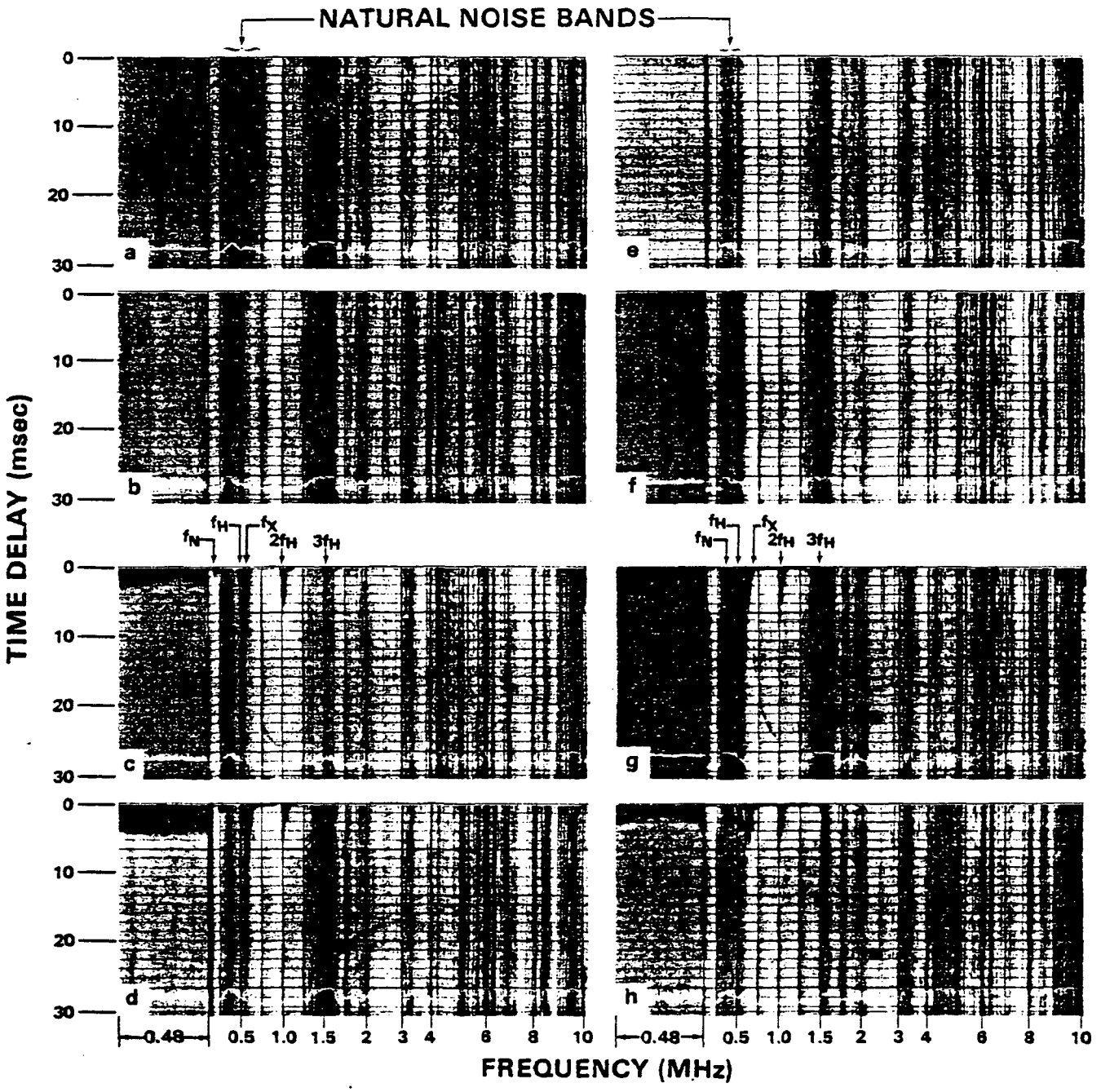

Figure 12. Natural Z mode noise observed on 8 consecutive ISIS 1 ionograms both when the sounder-transmitter was off (a, b, e and f) and on (c, d, g and h). The sounder-stimulated resonances and f_x cutoffs corresponding to the latter conditions are identified above ionograms c and g. The resonance between f_H and f_x on these ionograms corresponds to f_T. The satellite altitude, invariant latitude and magnetic local time ranged from 2734 km, 57° and 0045 in a to 2606 km, 53° and 0048 in h over Ottawa, Ontario (24 May 1974, 0709 to 0711 UT with 18 sec between ionograms).

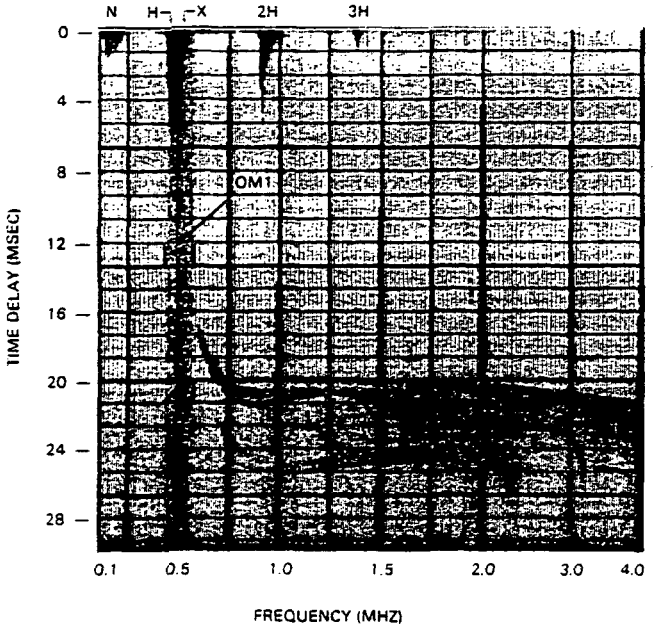

Figure 13. An example of ordinary mode AKR with minimum frequency clearly less than the extraordinary mode cutoff f_X (designated by X) (the frequency difference is 450 kHz) and maximum frequency clearly greater than f_T (which is between f_H, designated by H, and f_X) (the frequency difference in this case is 120 kHz). Second harmonic AKR, which is difficult to detect on this reproduction, was more prominent on adjacent ionograms. (8 August 1969, 0837 UT, 53°S, 178°W, 3350 km, 2136 MLT, 64° f_N/f_H = 0.37.)

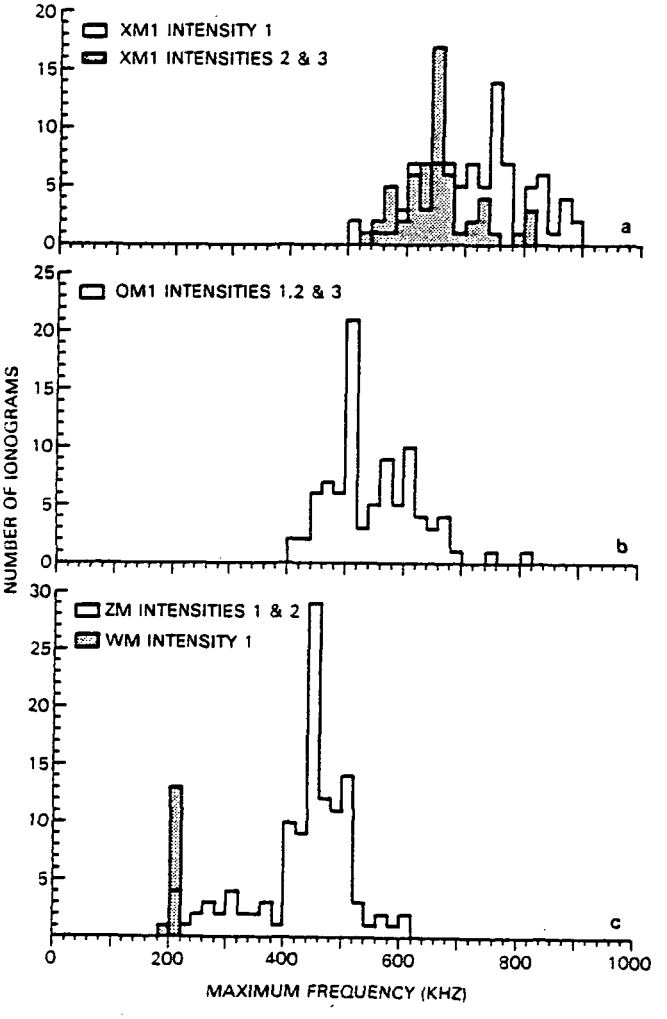

Figure 14. Histograms of the maximum observed frequencies for each of the fundamental AKR modes. These maximum frequencies include the frequency component structure within a given signal. The signal was tabulated according to the intensity of the maximum frequency component even when a lower frequency component was of higher intensity, a condition often encountered (30%) in the XM1 intensity 1 data in a.

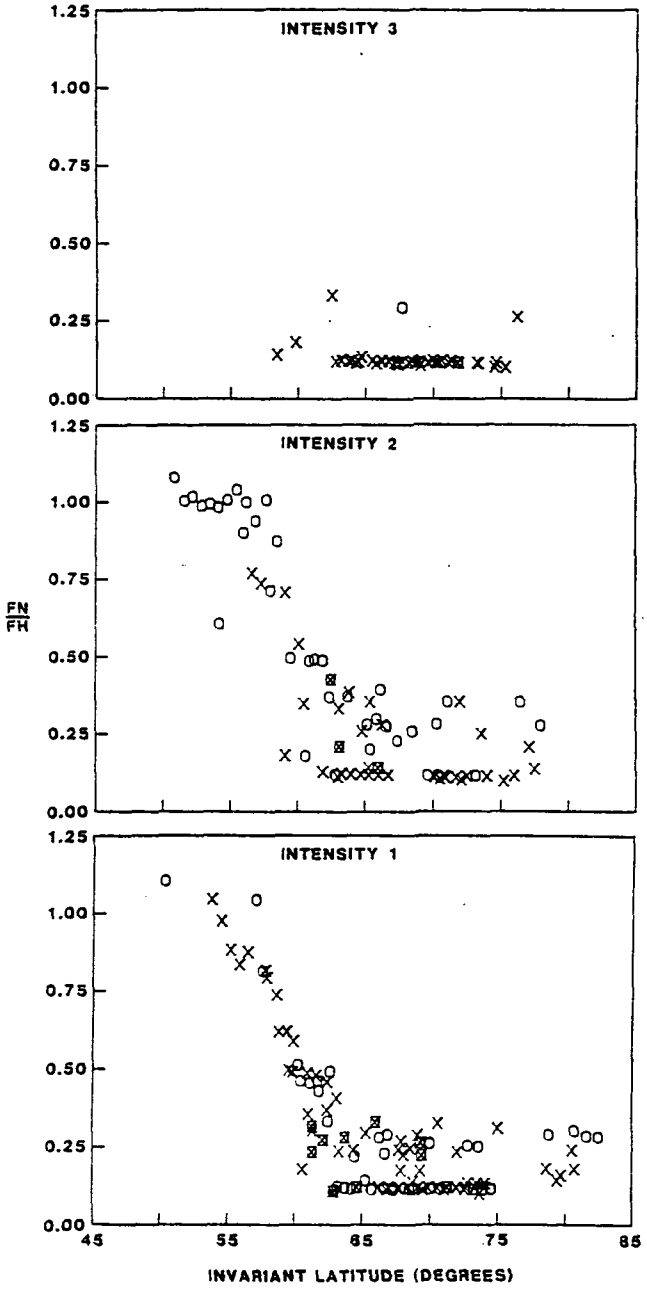

Figure 15. Invariant latitude and f_N/f_H values as measured at the point of reception of X and O mode AKR by signal intensity. (The intensity of the minimum frequency component was used for this presentation when frequency component structure was observed.)

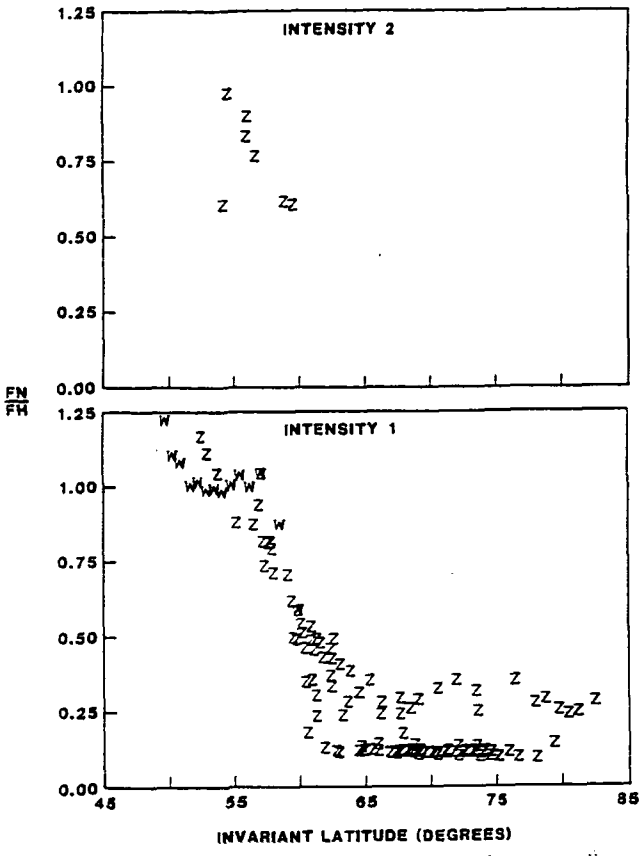

Figure 16. Same as Figure 15 for the Z and W modes.

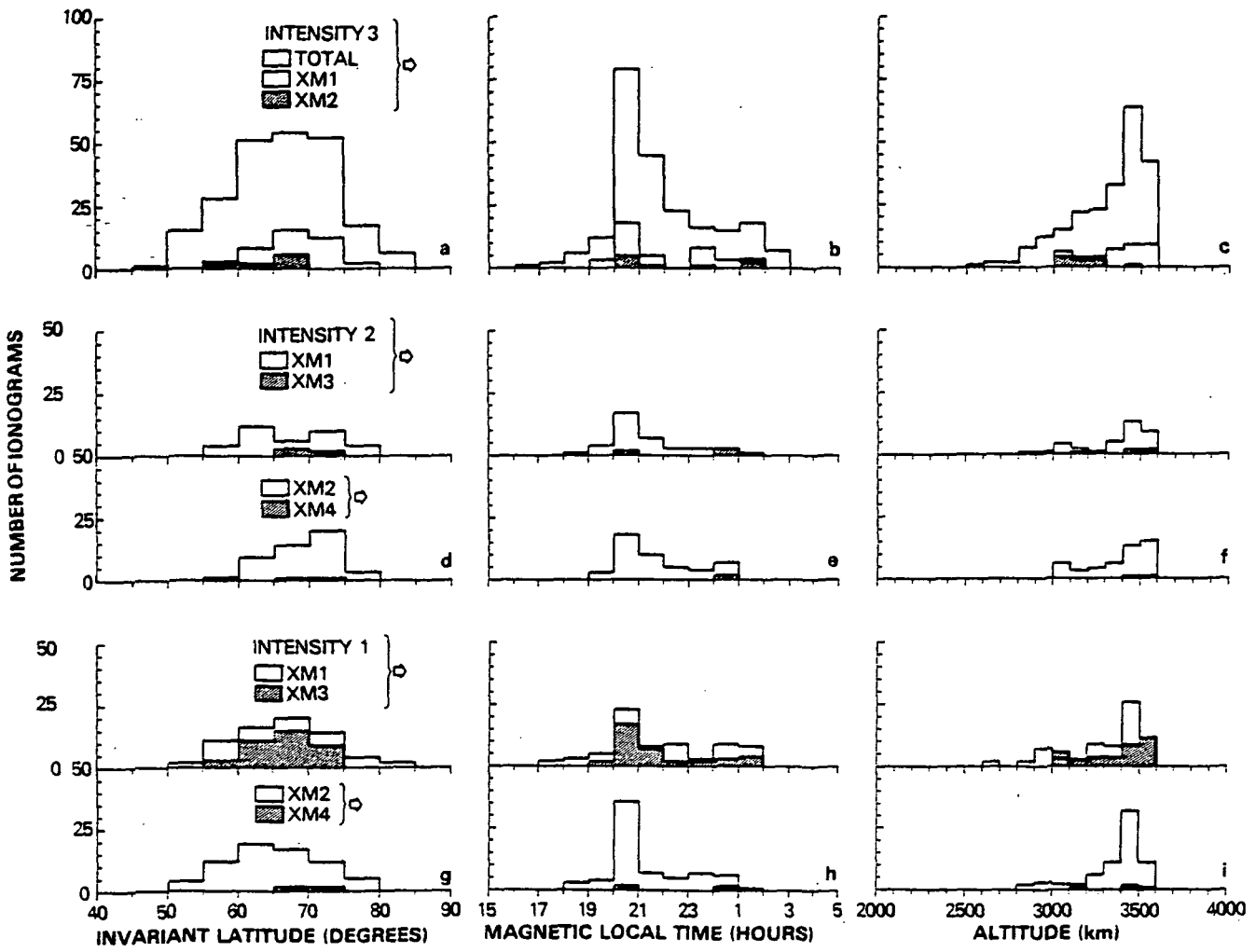

Figure 17. Distributions of fundamental and harmonic X mode AKR data in terms of the satellite Λ (a, d and g), MLT (b, e and h) and h (c, f and i) at the point of signal reception. Separate distributions are presented for each signal intensity level. As in Figures 15 and 16, this designation is based on the minimum frequency component when frequency component structure was present.

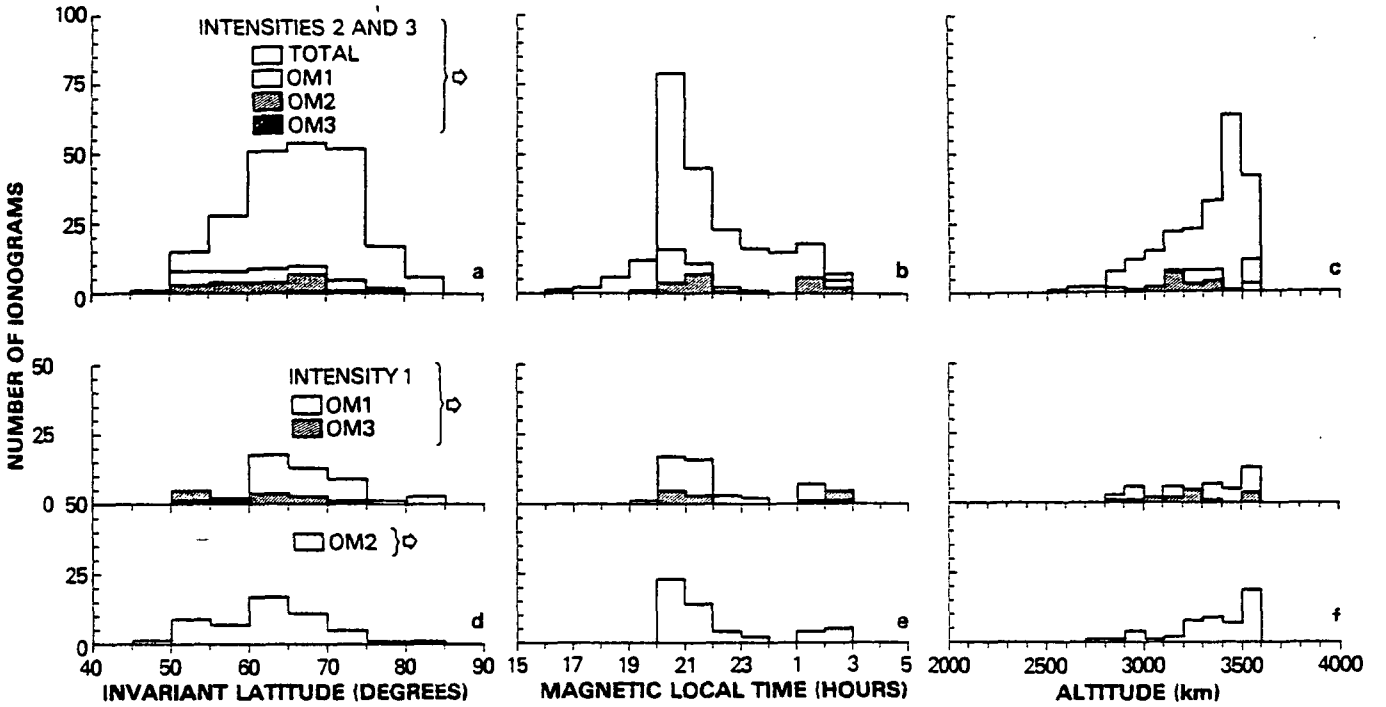

Figure 18. Same as Figure 17 except for the O mode AKR data.

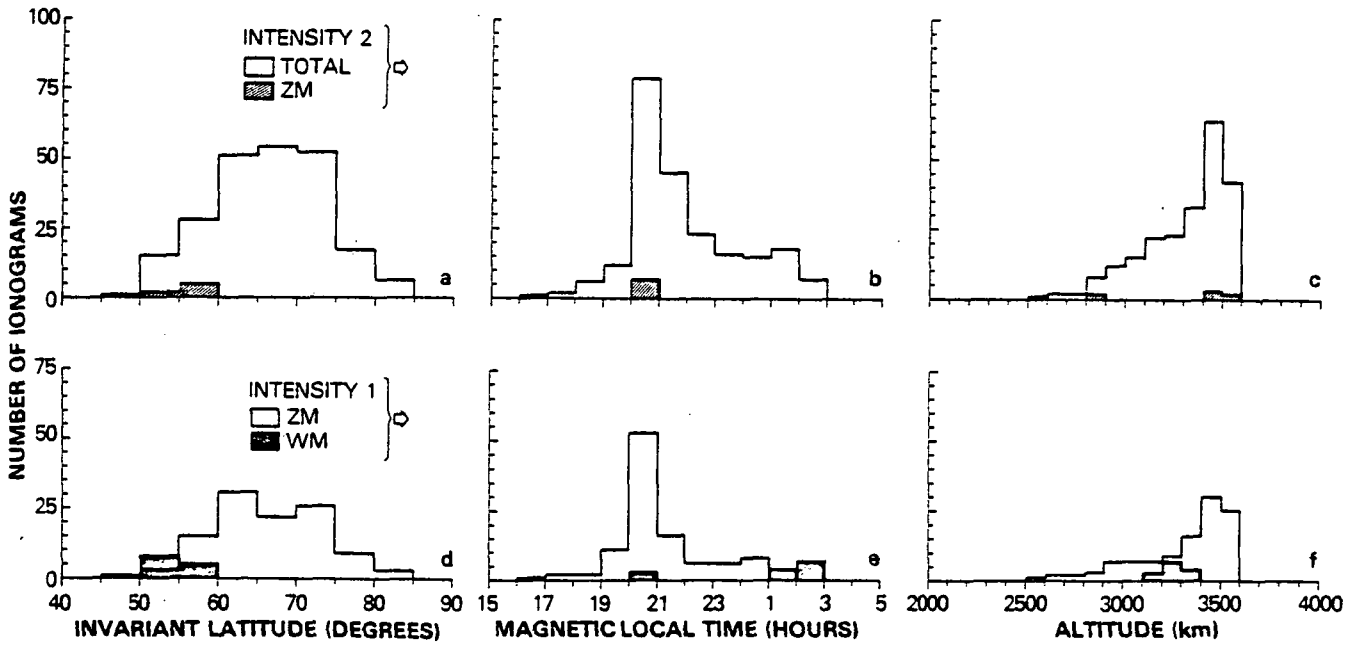

Figure 19. Same as Figure 17 except for the Z and W mode data.

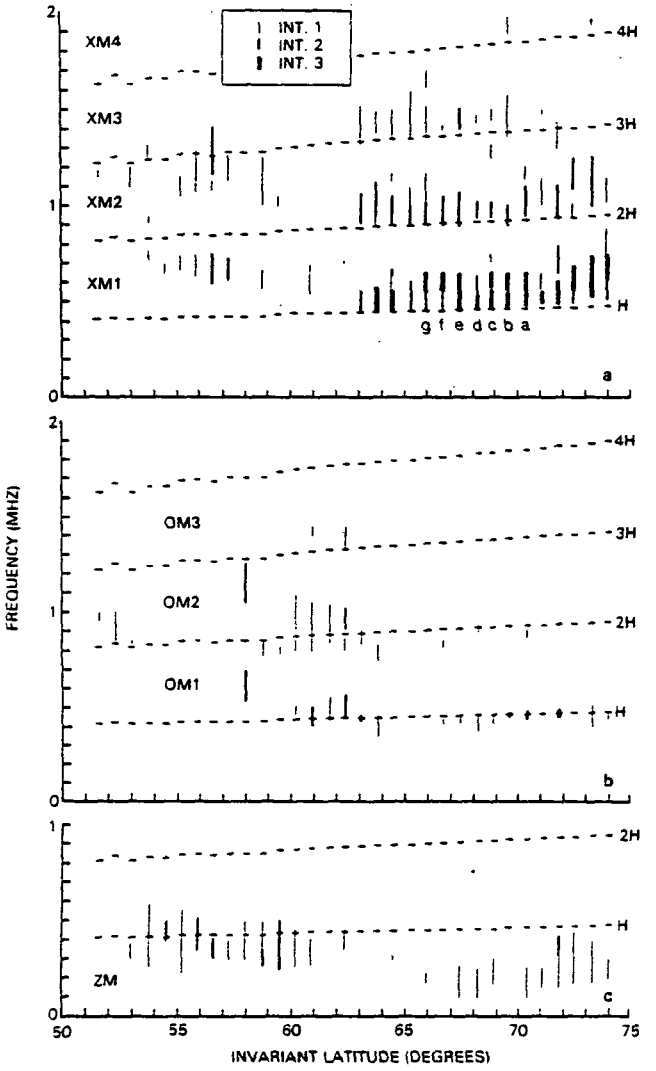

Figure 20. Frequency bandwidths for X, O and Z mode AKR against Λ (for the ISIS 1 pass of 19 August 1969 in Table 1) in frames a, b and c, respectively. The XM1 bands identified as a-g in frame a correspond to specific features to be discussed in connection with Figures 26 and 27. (Note: the time interval and geographic latitude range given for this pass in Table 1 corresponds to the first 21 data columns in from the right side on frames a, b and c).

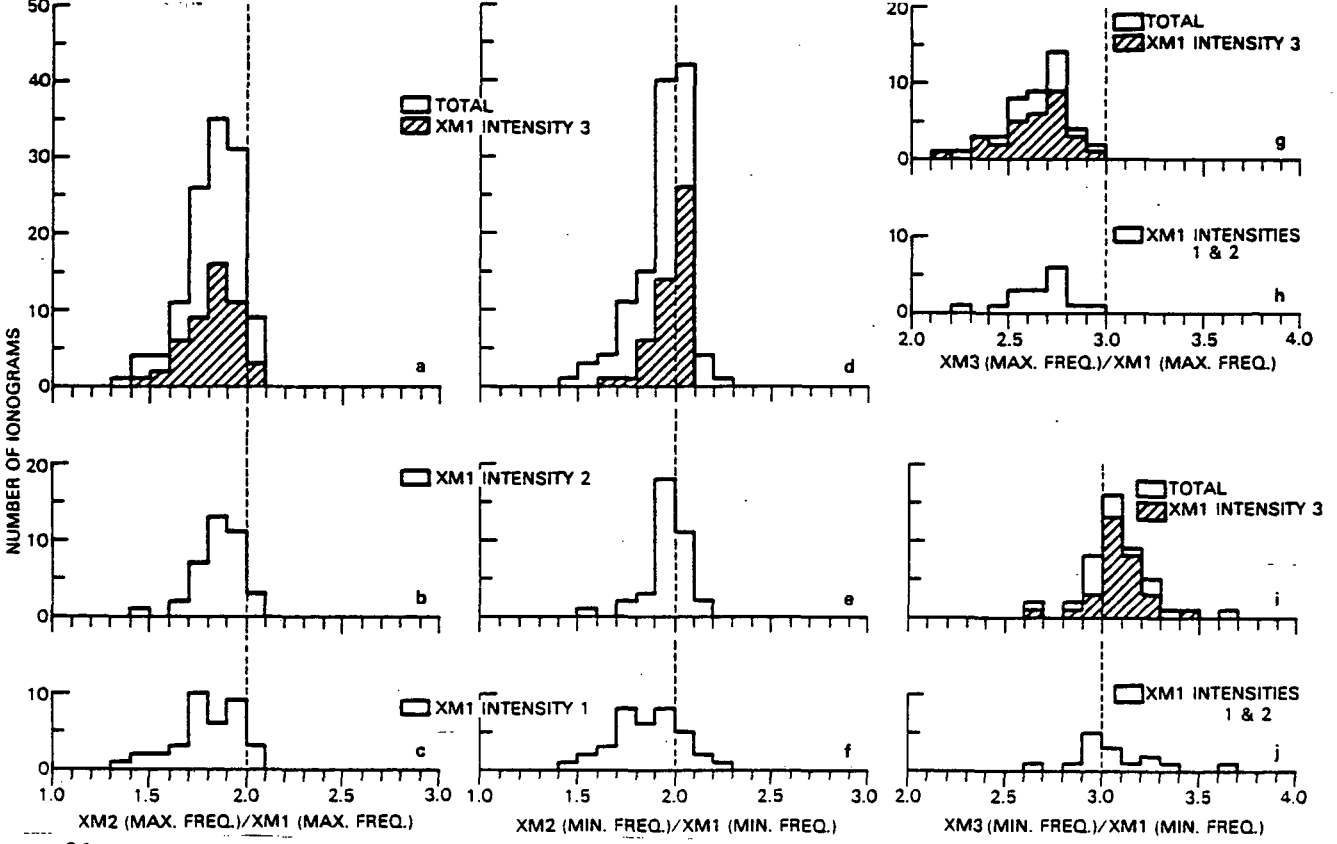

Figure 21. Ratios between harmonic and fundamental X mode AKR frequencies grouped by the intensity observed on the fundamental. Second harmonic to fundamental maximum frequencies in a, b and c and minimum frequencies in d, e and f; third harmonic to fundamental maximum frequencies in g and h and minimum frequencies in i and j.

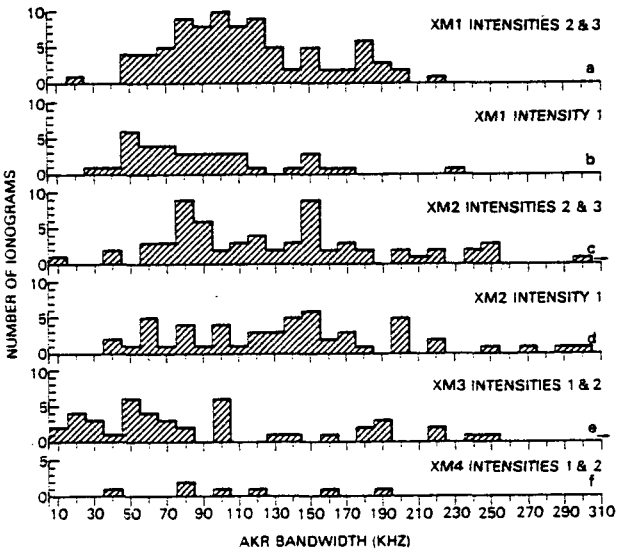

Figure 22. Distribution of frequency bandwidths observed on X mode fundamental and harmonic AKR by signal intensity. The arrows in c and e indicate off-scale values (one value at 360 kHz and one at 380 kHz in c and one at 400 kHz in e).

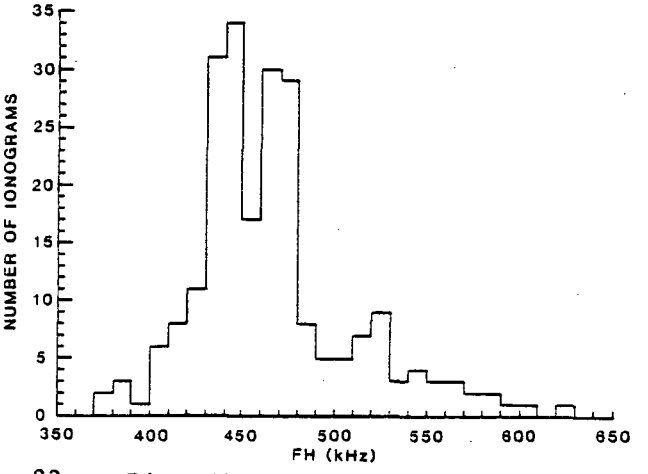

Figure 23. Distribution of ambient f_H values corresponding to the ISIS 1 data of Figure 1.

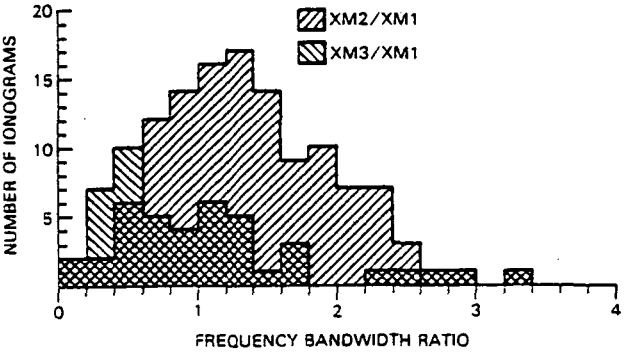

Figure 24. Distribution of AKR frequency bandwidth ratios (2nd and 3rd harmonics to the fundamental) from ISIS 1 ionograms containing fundamental and harmonic X mode AKR.

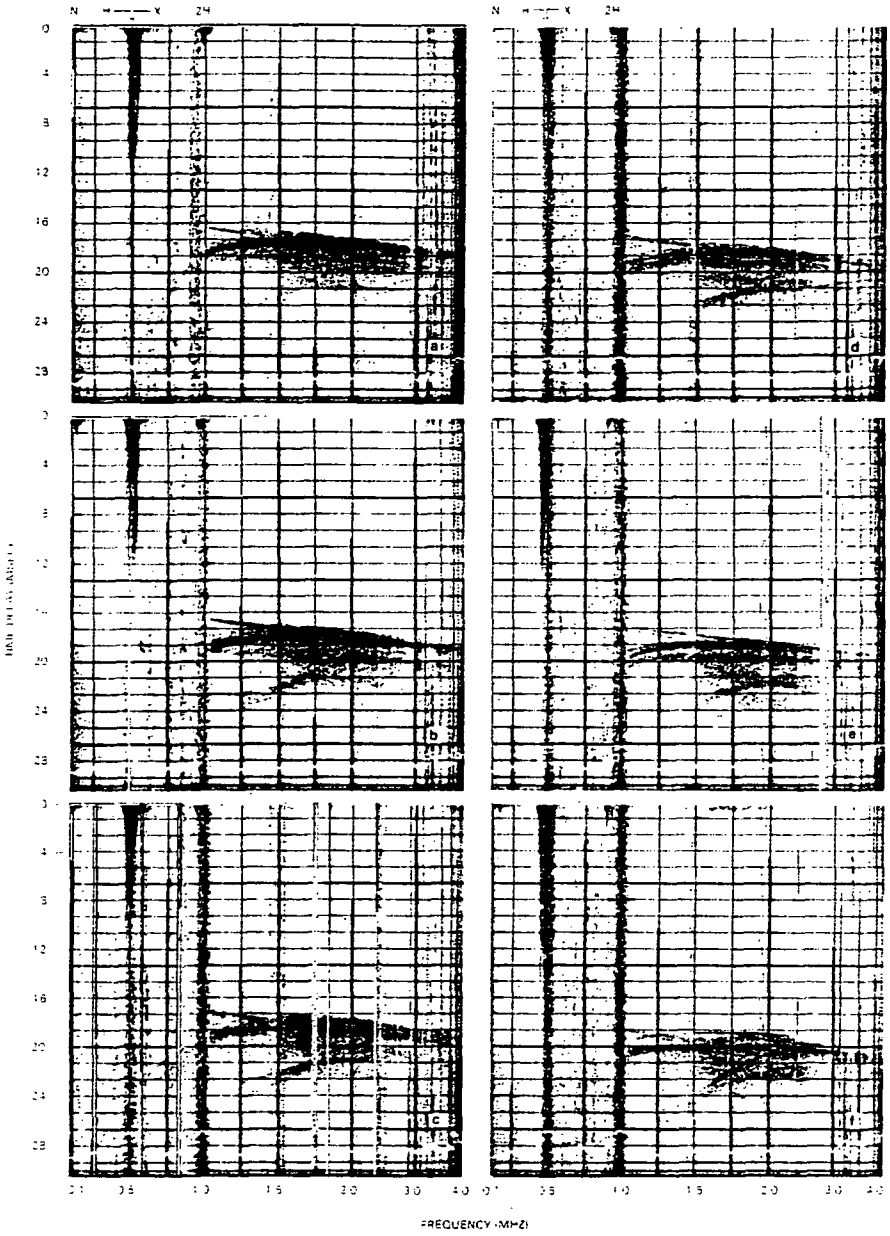

Figure 25. Second harmonic AKR observed on 6 consecutive ionograms (signal near 1.0 MHz covering all time delays). The intensity of these signals are greater than the fundamental AKR (signals near 0.5 MHz covering all time delays) on a-e. (Note: the long-duration sounder-stimulated electrostatic resonance at f_H contributes to the AGC response near 0.5 MHz on each ionogram.) The satellite altitude, invariant latitude and magnetic local time ranged from 2972 km, 62° and 0136 in a to 3084 km, 58° and 0142 in f over Fairbanks, Alaska (31 October 1969, 1353 to 1355 UT with 28 sec between ionograms, f_N/f_H = 0.26 in a, 0.30 in b, 0.17 to 0.18 in c-f).

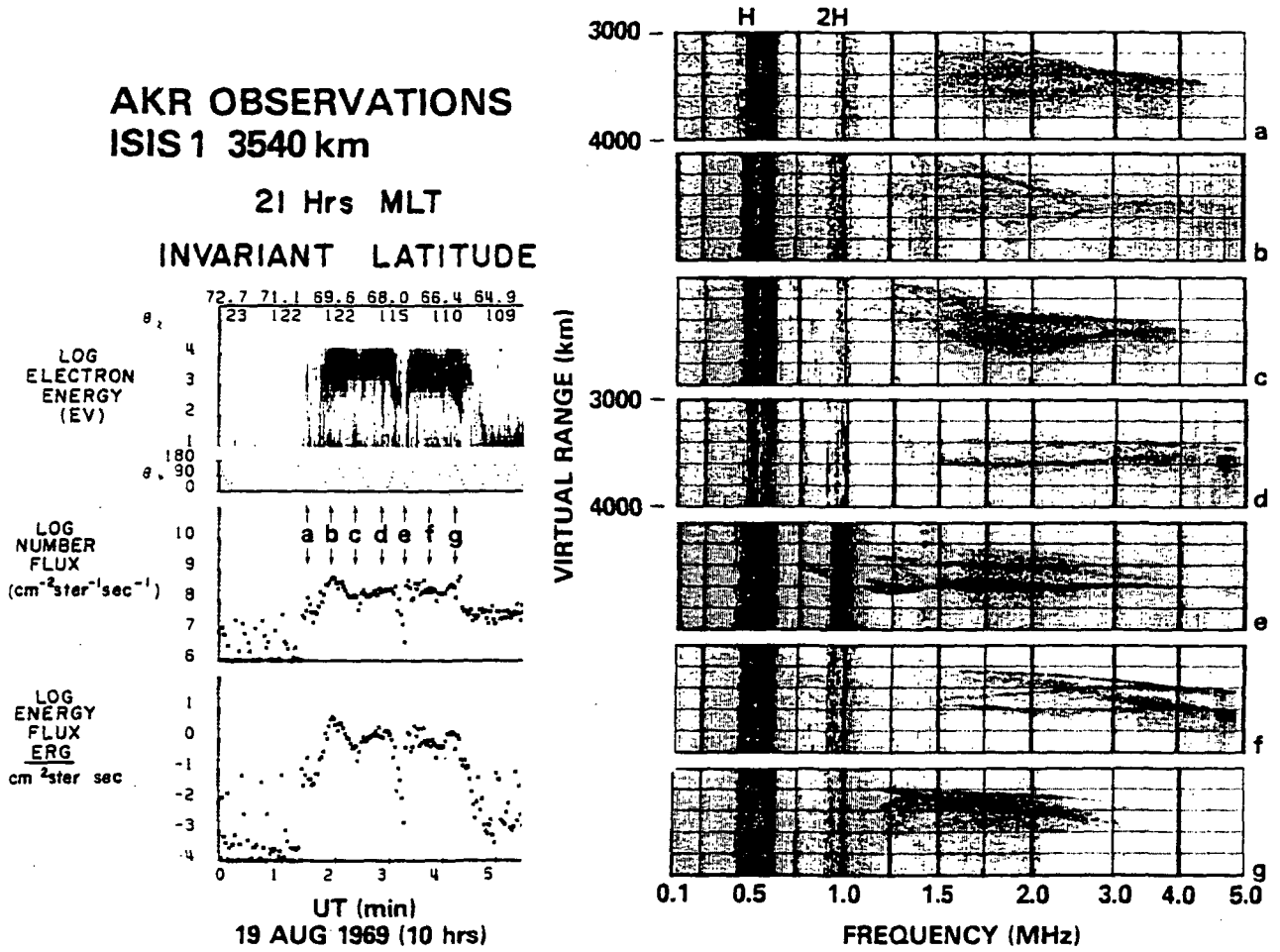

Figure 26. ISIS 1 soft particle spectrometer SPS data (left) and ionogram data (right) corresponding to the pass used in Figure 20. The UT and Λ values corresponding to the ionogram samplers on the right, each 1000 km in virtual range (or 6 2/3 msec of time delay), are identified in the SPS data at the left and in the frequency scaling presentation of Figure 20a, respectively ($f_N/f_H \leq 0.11$.)

Figure 27. Bottom: sounder-derived N_e contours (10^2, 3 x 10^2, 10^3, 3 x 10^3, etc.), field-aligned projections through X mode AKR source encounters (with projected lower extent of source region indicated) and AKR intensity information for the ISIS 1 data of Figures 20 and 26; middle and top: cylindrical electrostatic probe data for two 30 sec time intervals.

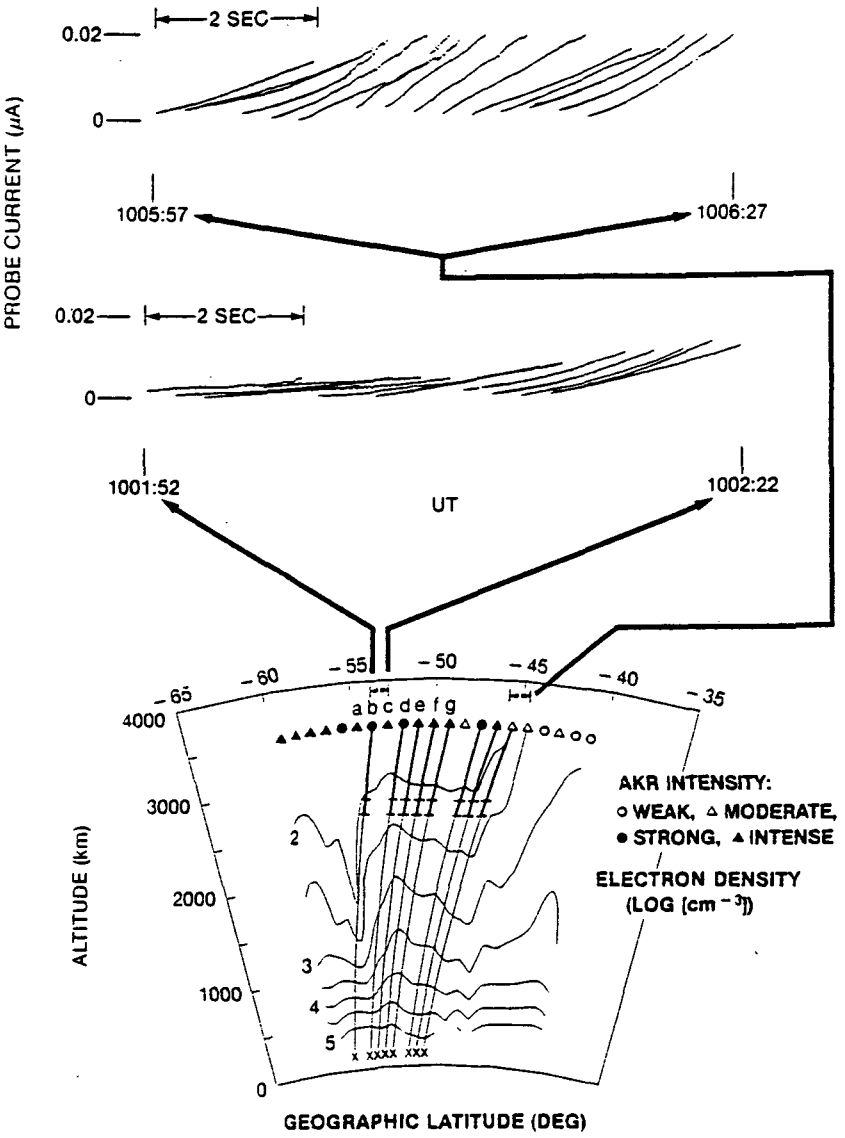

Figure 28. Electron density contours (log [cm^{-3}]) and AKR information (as in Figure 27) obtained from ISIS 1 AKR source region traversals during 6 of the 12 passes in Table 1: 26 Nov 1969 (a), 17 August 1969 (b), 7 August 1969 (c), 3 August 1969 (d), 6 November 1970 (e) and 8 August 1969 (f).

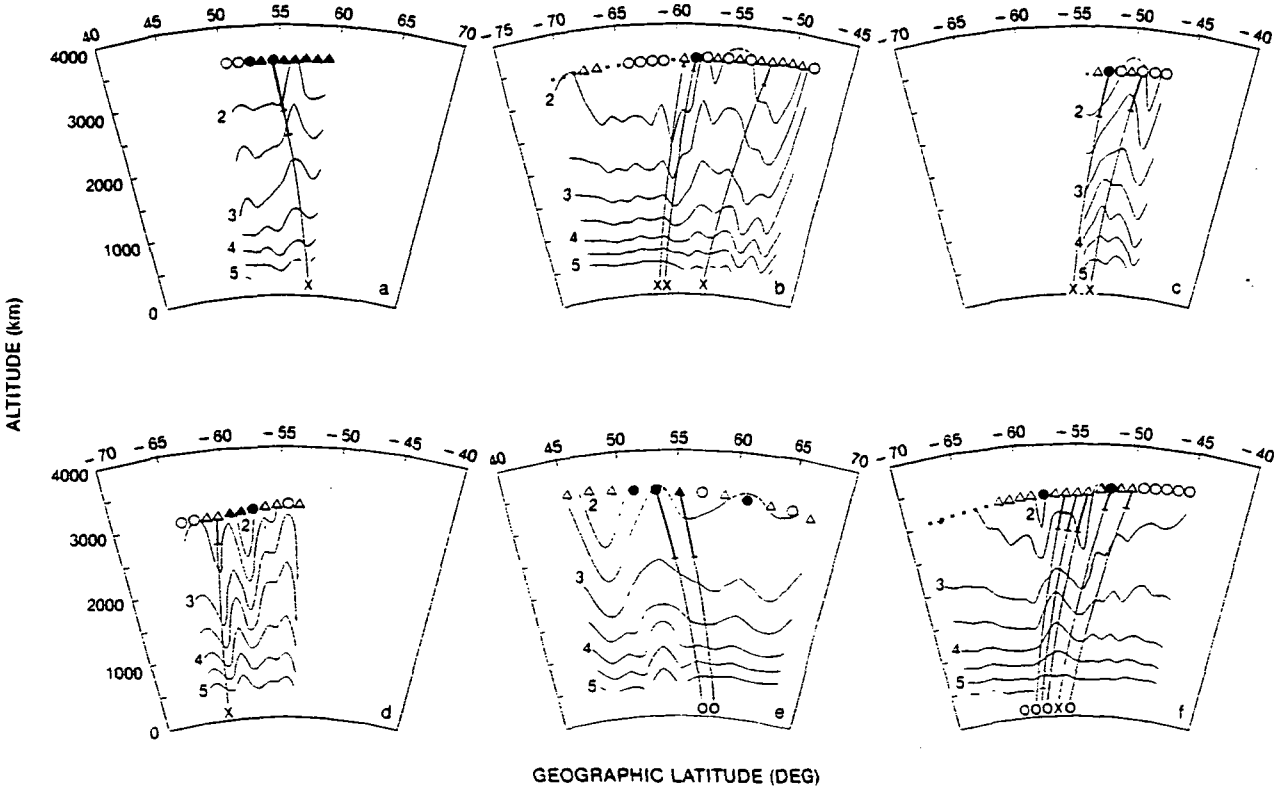

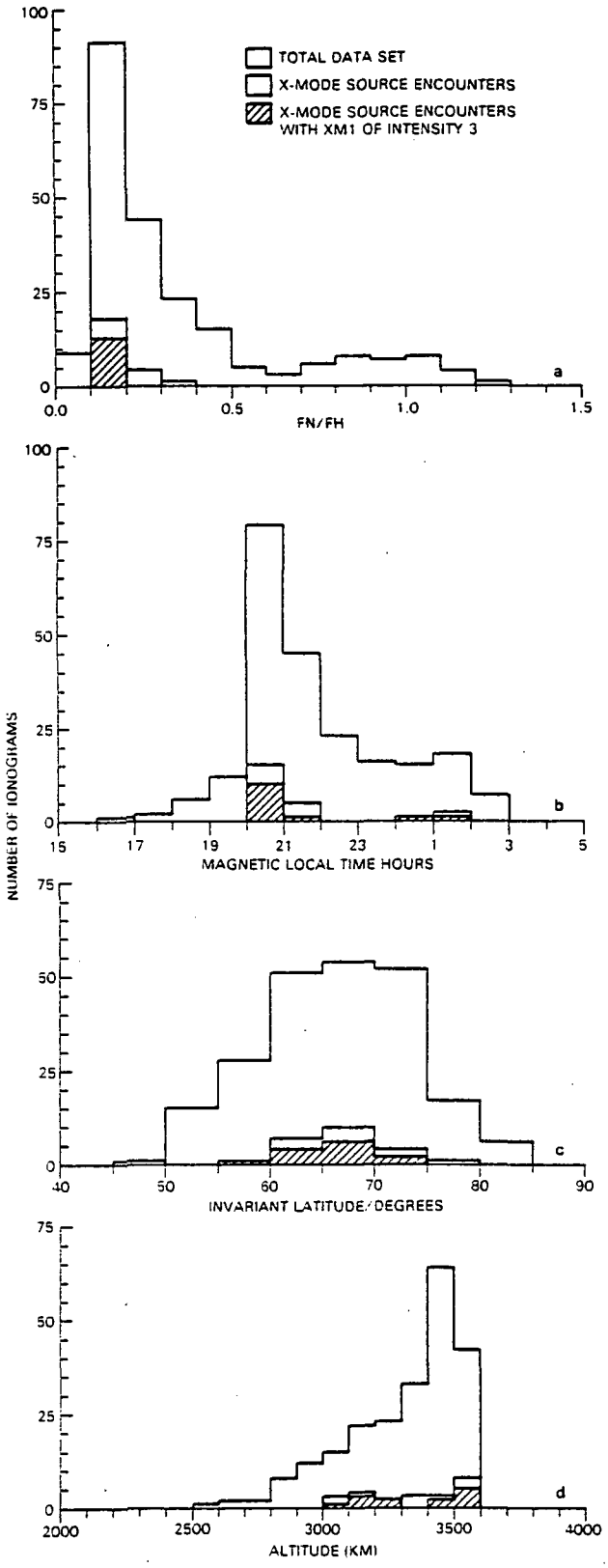

Figure 29. Distribution of ISIS 1 X mode AKR source region encounters in f_N/f_H (a), MLT (b), Λ (c) and h (d). See the comment at the end of the Figure 9 caption pertaining to the 0 to 0.2 f_N/f_H values in (a).

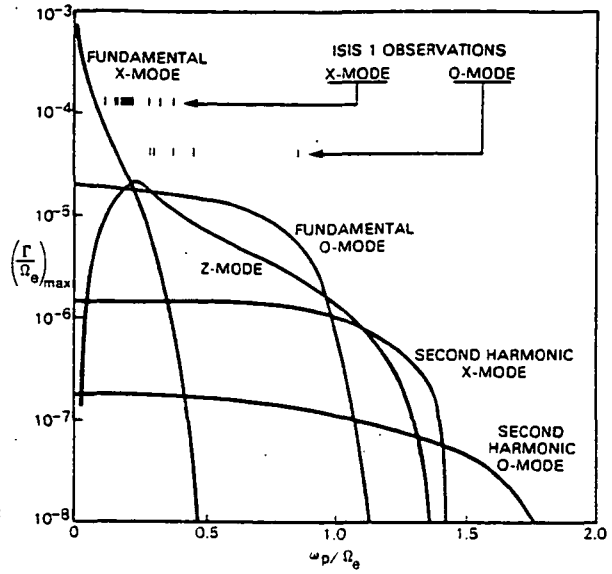

Figure 30. ISIS 1 projected AKR X and O mode source region $(f_N/f_H)_{max}$ values compared with theoretical normalized maximum temporal growth rates $(\Gamma/\Omega_e)_{max}$ of Melrose et al. [1984].

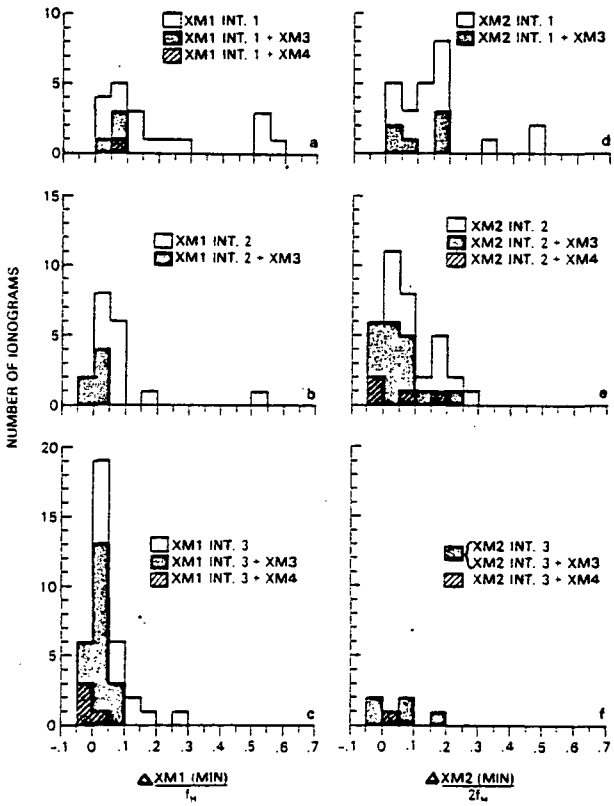

Figure 31. Distribution of frequency gaps $\Delta XM1(min) = XM1(min) - f_H$ (a, b and c) and $\Delta XM2(min) = XM2(min) - 2f_H$ (d, e and f) by intensities of XM1 and XM2, respectively.

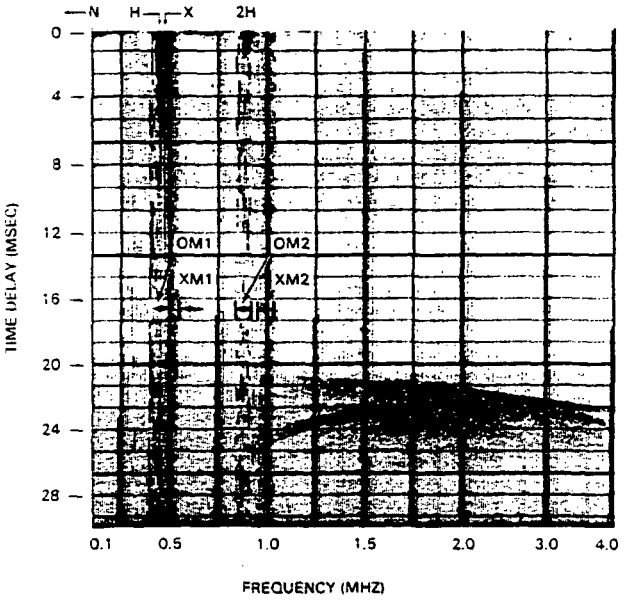

Figure 32. ISIS 1 ionogram illustrating the distinction between OM2 and XM2 signals (17 August 1969, 0848 UT, 53°S, 170°E, 3529 km, 2100 MLT, 66° Λ, f_N/f_H = 0.13.)

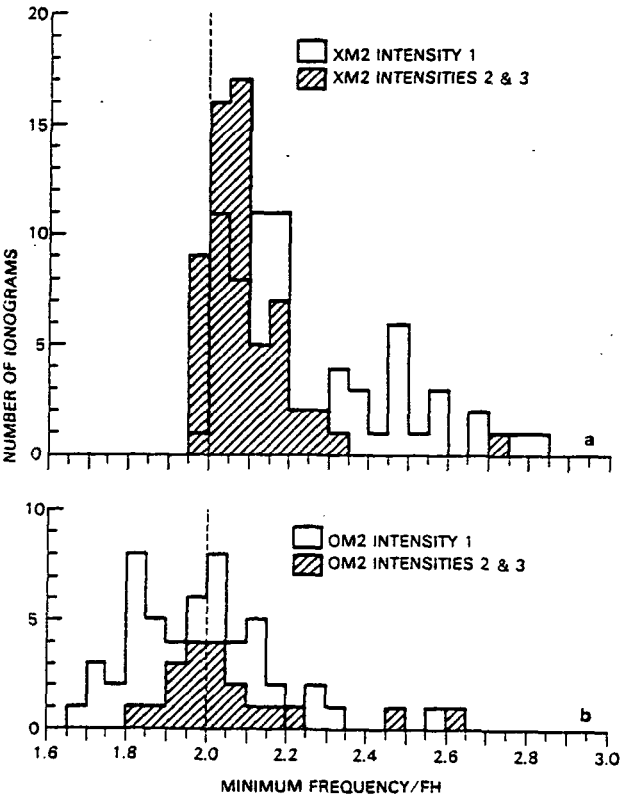

Figure 33. Distributions of the ratios of XM2 minimum frequencies to f_H (a) and OM2 minimum frequencies to f_H (b) by signal intensities.

BIBLIOGRAPHIC DATA SHEET

1. Report No. TM 86101	2. Government Accession No.	3. Recipient's Catalog No.
4. Title and Subtitle: AURORAL KILOMETRIC RADIATION: WAVE MODES, HARMONICS AND SOURCE REGION ELECTRON DENSITY STRUCTURES		5. Report Date: May 1984 6. Performing Organization Code
7. Author(s): Robert F. Benson		8. Performing Organization Report No.
9. Performing Organization Name and Address: NASA/Goddard Space Flight Center, Greenbelt, MD 20771		10. Work Unit No. 11. Contract or Grant No.
12. Sponsoring Agency Name and Address: NASA/Goddard Space Flight Center, Greenbelt, MD 20771		13. Type of Report and Period Covered: Technical Memorandum 14. Sponsoring Agency Code

15. Supplementary Notes

Submitted for publication to Journal of Geophysical Research

16. Abstract

A change from extraordinary (X) mode to ordinary (O) mode dominance is observed in the auroral kilometric radiation (AKR) detected on ISIS 1 topside sounder ionograms as the source region plasma to gyrofrequency ratio f_N/f_H varies from 0.1 to 1.3. In addition to the X and O mode AKR, Z (the slow branch of the X mode) and whistler (W) mode are also observed. The Z mode is typically slightly less intense than the O mode. The W mode is confined to frequencies less than $f_H/2$, suggesting that it is the result of field-aligned ducted signals reaching the satellite from a source at lower altitudes. Harmonic AKR bands are commonly observed and the 2nd harmonic appears to be due to propagating signals. The deduced $(f_N/f_H)_{max}$ at the bottom of the AKR source region is always less than 0.4 and is typically less than 0.2 during the generation of X-mode AKR, but approaches 0.9 for O-mode AKR. No large density enhancements were observed within AKR source region density cavities. These observations provide additional confidence that the observed intense AKR is cyclotron X-mode radiation rather than plasma frequency O-mode radiation.

17. Key Words (Selected by Author(s))	18. Distribution Statement
Auroral kilometric radiation, Planetary radio emissions, electron density cavity, ISIS 1	

19. Security Classif. (of this report)	20. Security Classif. (of this page)	21. No. of Pages	22. Price*
U	U	75	

*For sale by the National Technical Information Service, Springfield, Virginia 22151.